Ultrasound optical tomography for imaging in the human brain

Paulina Tatidis

Master's Thesis

Supervisors

Akvilė Zabiliūtė-Karaliūnė
Adam Kinos
Eglė Bukartė

Examiner

Cord Arnold

LUND
UNIVERSITY

Abstract

Ultrasound optical tomography is a medical imaging modality that combines ultrasound and light to improve the low resolution of optical imaging caused by scattering in tissue. Photons passing through an ultrasound pulse have a probability of being frequency shifted. By filtering out these photons and analysing them, images with optical contrast and ultrasound resolution can be obtained.

In this thesis the conditions for ultrasound optical tomography inside the human brain, both infant and adult, are investigated. Possible applications include imaging of brain tumours or stroke imaging. The investigation includes experimentally characterizing an ultrasound pulse after propagating through a slab of skull bone, originating from an infant cranium, as well as using Monte Carlo simulations of photon propagation to estimate signal strengths and signal-to-noise ratios from different depths in the head. Based on measurements, an acoustic energy attenuation of about 80-90% was estimated to take place in the skull bone, however the pulse shape did not appear severely distorted. For the simulations, realistic head models were created using optical parameters found in the literature, and penetration depths for imaging were estimated to be ≤ 2 cm in the adult head and ≤ 3 cm in the infant head, given perfect filtering of the frequency-shifted photons. The depths correspond to reaching superficial white matter in the adult head, and going well into the white matter in the infant head. The calculations were based on the assumption that the probability of frequency-shifting experienced by a photon is proportional to the pathlength spent inside the ultrasound pulse volume. This assumption was then evaluated by comparing estimates to simulations of ultrasound-light interaction.

Though the conditions seem challenging for imaging of the adult head, several aspects of the setup can be improved. These include the surface areas of the light source and detector, the powering voltage of the ultrasound transducer, and the time during which signal is collected. If real time imaging is compromised, the penetration depth would be increased. The location at which imaging is performed also affects the size of the signal, as the thicknesses of tissue layers vary across the head. Lastly, there is some uncertainty regarding the optical parameters chosen in the simulation, which would greatly affect the result.

Populärvetenskaplig sammanfattning

Att använda ljus som medium för bildteknik ter sig nog intuitivt för de flesta, eftersom det är ljus som låter våra ögon se bilder av omgivningen. Tack vare ljus är världen omkring oss synlig i en mångfald av färgnyanser, som ger oss information som hade gått förlorad i svartvitt. En blick av de rödsprakande löven utanför fönstret påminner oss snabbt om tiden på året, och färgen av ett äpple kan avgöra huruvida det är omoget eller ruttet. Är det då inte synd att våra läkare, för diagnostik, inte kan betrakta inre vävnader i färg utan att i vissa fall mödosamt tränga in en kamera, eller skära ut ett prov från kroppen?

Svårigheten med att använda ljus för avbildning av inre vävnad ligger i att ljus kraftigt och slumpmässigt sprids i kroppen. En foton som skickats in i vävnad byter slumpmässigt riktning många gånger om, vilket resulterar i en helt oförutsägbar färd. En kamera eller detektor som samlar in fotoner efter att de vistats i kroppen kan därför inte återskapa en högupplöst bild av den inre vävnaden.

Ultrasound optical tomography (UOT) är en bildteknik som just nu utvecklas för att lösa problemet med låg upplösning på grund av ljusets spridning i vävnad. Som namnet antyder används optisk strålning, det vill säga ljus, tillsammans med ultraljud för att skapa bilder. Ultraljud används ju redan inom sjukvården för att göra (svartvita) bilder, men inom UOT används det endast för att härleda ett av områdena i vilket ljuset vistats. Ljus som färdas genom ett område med ljudvågor har nämligen en sannolikhet till en liten förändring av sin frekvens, det vill säga av sin färg. I UOT skickas en liten ultraljudspuls in i vävnaden, till en känd position, samtidigt som vävnaden belyses med ljus. En bråkdel av fotonerna kommer i sin slumpmässiga väg att färdas genom ultraljudspulsen, och kan då bli frekvensskiftade. När en detektor sedan samlar in ljuset kan de fotoner som färdats genom det kända området urskiljas med hjälp av frekvensfilter. Genom att variera positionen av ultraljudspulsen återskapas en bild av vävnaden, pixel för pixel. Upplösningen är därmed räddad, och fotonerna som detekteras bär på intressant information om vävnadens färg.

Eftersom UOT är en teknik som fortfarande utvecklas är det ännu inte fastställt i vilka vävnader den fungerar bäst. I denna masteruppsats undersöks möjligheterna för avbildning av hjärnvävnad med UOT. Två viktiga omständigheter som avgör teknikens genomförbarhet är ljusets spridning och absorption i huvudet, samt det ultraljudsfokus som går att uppnå genom skallben. Här presenteras resultat av en experimentellt uppmätt ultraljudspuls som färdats genom en bit skallben, tillsammans med resultat från ett antal simuleringar av fotoners slumpmässiga vägar i huvudet, genom hud, ben och hjärnvävnad. Mer specifikt jämfördes simuleringar mellan ljus i ett spädbarnshuvud och ljus i ett vuxet huvud.

Mätningarna visar en ca. 80-90 procentig energiförlust hos ultraljudet då det färdas genom skallbenet. Resultat från simuleringarna visar också att förhållandena för avbildning är bättre i spädbarnshuvudet än i det vuxna huvudet, vilket troligtvis beror på spädbarnets tunnare skalp och skallben. För det vuxna huvudet tycks förhållandena för avbildning utmanande, men eftersom det fortfarande finns en osäkerhet i simuleringarna, och eftersom flera förbättringsområden inte utforskas i detta arbete, krävs vidare undersökning.

Acknowledgements

Contents

1 Introduction

In the age of modern medicine, deep tissue imaging plays a large role in diagnostics within many medical fields. Over the past 200 years different imaging modalities have been developed, from ultrasonography to magnetic resonance imaging, all with their own set of advantages making them suitable for different settings. Some modalities use electromagnetic radiation, such as the well known technique of radiography, or X-ray imaging, which uses high energy radiation with wavelengths ranging from 10 pm to 10 nm. Another example is optical imaging, where radiation in the optical wavelength range, or what is in everyday language called light, is used.

We can intuitively understand that light is useful for imaging as it allows our eyes to visualize our surroundings. Beyond this intuition though, light can be particularly useful for investigating the molecular contents of tissue, as most tissue contains molecules with absorption spectra in the optical wavelength range. Therefore many interesting properties of tissue may be uncovered in images made with optical contrast. One example is the concentrations of oxygenated and deoxygenated haemoglobin. Both molecules have different absorption spectra in the 200-900 nm wavelength range, and the ratio between their concentrations reveals the oxygen saturation level in tissue, which is useful when investigating local blood supply.

A large problem with optical imaging, however, is the fact that light is heavily scattered in soft tissue. A photon propagating through the tissue randomly changes its direction many times over, before exiting and being captured by a detector. Thus, the resolution of optical images becomes poor. One imaging technique that works around this issue is ultrasound optical tomography, which will be described in further detail in section 1.1. In ultrasound optical tomography, probing light interacts with an ultrasound pulse focused into a known position inside the tissue, to generate slightly frequency-shifted light. Only light that has passed through the ultrasound focus volume is frequency shifted. Thus, by scanning the tissue with the ultrasound images can be reconstructed with optical contrast, but with spatial resolution given by the ultrasound.

This thesis investigates the conditions for ultrasound optical tomography inside the human head, using experimental measurements of the transmission of ultrasound pulses through the skull bone, as well as Monte Carlo simulations of light propagation and ultrasound interaction. The aim and contents of the thesis will be described in detail in section 1.2.

1.1 Ultrasound optical tomography

Ultrasound optical tomography (UOT) is an imaging modality that combines light and ultrasound to produce high resolution images in deep tissue, despite its scattering properties. The principle is illustrated in Figure 1, which will be referenced as the technique is explained in detail. But let us first shortly describe why its two main components, ultrasound and light, are both useful for tissue imaging.

Ultrasound, which refers to sound waves with frequencies above the human hearing range (that is above 20 0000 Hz [1]), is already used for tissue imaging in ultrasonography – a well established technique that can achieve spatial resolutions in the μm scale. However, ultrasound alone only distinguishes between materials with differences in acoustic impedance. Optical imaging on the other hand, has the potential to produce images in color by combining probing wavelengths, and is suitable for visualizing soft tissues as they absorb and scatter light in a great variety of ways. However, light has the previously mentioned limitation of being heavily scattered in tissue, which

quickly ruins image resolution at depths beyond a few millimeters.

In UOT, the idea is to let an ultrasound pulse, focused into a small volume with a known position inside the tissue, interact with probing light (shown as arrows in Figure 1). Although the ultrasound pulse also propagates through the tissue, the speed of light is so comparably large that it can be considered still during the time that the photons spend in the tissue. As the photons propagate through the insonified volume they have a probability of being frequency shifted by integers of the ultrasound frequency [2]. The theory of this acousto-optic interaction will not be described in detail here, but can be shortly explained as follows: Ultrasound, like all sound waves, constitutes a periodic displacement of the particles making up the medium within which it travels. The displacements also result in periodic changes of the medium's density. The moving particles are the same particles that scatter the photons propagating through the medium. Furthermore, the changing density implies a periodically changing refractive index in the medium. Both these phenomena cause periodic phase variations that modulate the frequency of light [2].
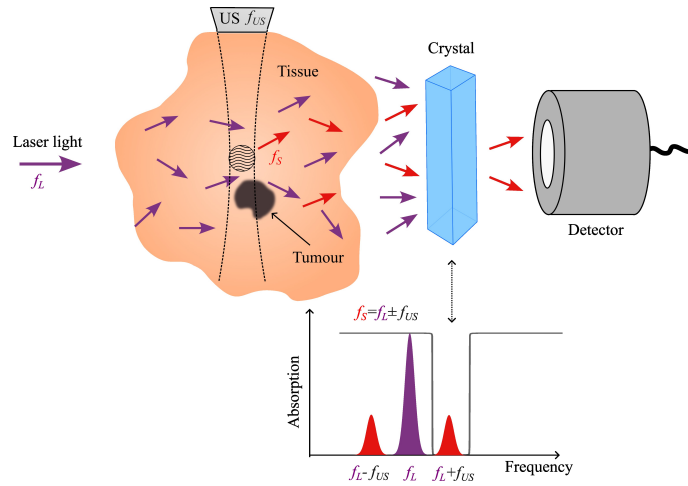
Figure 1: The principle of UOT imaging illustrated. Carrier photons of frequency f_L (illustrated as purple arrows) are irradiated into the tissue. As they pass through the ultrasound volume some of them are frequency shifted and become tagged photons (illustrated as red arrows). The new frequency is shifted by integers of the ultrasound frequency f_{US} – the first positive and negative sidebands are illustrated in the figure as red intensity peaks displaced from the purple intensity peak of at carrier frequency. The photons exit the tissue and pass through a crystal acting as a spectral hole burning filter that only transmits frequencies within a narrow window, as shown in the absorption spectrum in the image. The detector receives the filtered signal. Figure created by Akvilė Zabiliūtė-Karaliūnė and Maria Maria Ruchkina.

Therefore, as light from the tissue is detected, some of the photons that have propagated through the ultrasound focus volume have a frequency slightly different from the photons that have not. The frequency-shifted photons constitute the information carrying signal in UOT and are usually called *tagged photons* or *tagged light* (pictured as the red arrows in Figure 1). The rest of the photons are considered noise, and are referred to as *carrier photons* or *carrier light* (pictured as purple arrows in Figure 1). If the tagged photons can be filtered from the carriers, they would provide information of the absorption in the insonified volume [2]. By scanning through tissue

with the ultrasound pulse an image can be created pixel by pixel, with a resolution limited by the size of the ultrasound focal volume [2]. In short, the image would be made with optical contrast, but with a spatial resolution limited by the resolution of the ultrasound.

The Quantum Information group at the Division of Atomic Physics, Lund University (within which this thesis was written) uses spectral-hole burning filters (illustrated as the crystal with accompanying absorption spectrum in Figure 1 and described in further detail in Ref. [3]) to attenuate the carrier light and filter through the tagged photons. Current filters at UOT wavelengths can achieve an attenuation of 25 dB, but improvement is ongoing, and filters at other wavelengths can already achieve over 40 dB attenuation [2].

Several different applications for UOT have been suggested, one example being imaging of tumours in breast tissue, which is currently being explored by the group at Lund University. Another suggestion is imaging of oxygenation in brain tissue, which could have possible applications for stroke patients or patients with brain tumours.

1.2 Purpose of this work

The purpose of this work is to assess the conditions for UOT imaging of the brain. This includes estimating the signal-to-noise ratio and the number of tagged photons that can be detected from different depths of the brain. These measures partly depend on how light propagates through different types of tissue in the head, including brain matter, but it also depends on the achievable focus and intensity of the ultrasound pulse inside the brain. The light propagation in head tissues was studied using Monte Carlo simulations, and ultrasound pulses from a medical transducer currently used in UOT lab setups was experimentally characterized after propagating through a piece of human skull bone. Note that neither impact from the scalp, nor from any internal tissues on the ultrasound pulse was experimentally studied.

Some previous work on this topic has been conducted within the group, including Monte Carlo simulations of light propagation in the human head. However, there was much uncertainty regarding the optical parameters assigned to the tissues in this simulation, as large variations exist in the literature. This is an issue as the optical parameters largely determine the simulation results. Therefore this thesis includes a small review of literature on the optical properties of tissue in the head, particularly on those of brain matter.

The plan was to first measure and characterize the ultrasound pulse, then simulate light propagation inside the human head, and finally combine the simulated photon paths with a simple model of the ultrasound pulse created from the measurements, to simulate probing light being tagged. The results would show the size of the UOT signal and the signal-to-noise ratio from different depths. Scripts for simulation of light propagation and frequency tagging have previously been developed within the group [2] and were used in this work. The wavelengths currently used for UOT at Lund university are 794 nm and 689 nm, but in this work all simulated light is assumed to have a wavelength of 800 nm.

Finally, the thesis also aims to see possible differences in imaging capabilities between the adult and the infant head, as these differ in anatomy. These differences were only accounted for in the Monte Carlo simulations and not in the experimental part of the work, as only one piece of skull bone was used, which originated from an infant cranium.

2 Ultrasound measurements

This chapter concerns the experimental measurements that were made to characterize the ultrasound transducer and the effect of skull bone on pulse shape, amplitude and propagation. The chapter begins with a short description of sound propagation, including acoustic attenuation and nonlinear effects, in section 2.1, after which the experimental setup and measurement procedure are described in section 2.2 and 2.3. The results, including the spatial pressure distribution of the pulse, its frequency contents and its attenuation in water, are given in section 2.4, and finally, an analytic expression is constructed to model the pulse after passing through skull bone in section 2.5.

2.1 Ultrasound propagation

Much like light, acoustic waves attenuate as they propagate through any medium, including tissue. Apart from viscosity of the medium dampening the wave, scattering particles also contribute to the attenuation [1]. Refraction and reflection occur at boundaries between regions of differing acoustic impedances and also affect the propagation of a pulse through inhomogeneous media such as tissue [1]. The attenuation of ultrasound is commonly described by an attenuation coefficient α, with unit dB/cm or sometimes dB/(cm MHz), when the attenuation increases linearly with the sound frequency. In this thesis the energy attenuation will be discussed, and the coefficient α will refer to the relation shown in Equation 1:

$$E(z) = E_0 \times 10^{-(\alpha/10)z} \, , \tag{1}$$

where E is the energy of a sonic pulse with initial energy E_0 after propagating a distance z in a medium with attenuation coefficient α [1].

Although acoustic attenuation can be described analogously to optical attenuation, one phenomenon specific to acoustic waves will be discussed in conjunction with our measurements, namely the nonlinearity of ultrasound propagation. A simple acoustic wave generated in a sinusoidal shape will have different phase speeds at different points on the wave shape [4]. This is because the phase speed of sound depends on the density of its medium. The speed is larger in higher density media, and smaller in lower density media, and as the wave corresponds to an oscillation of the medium's density, the phase speed varies over positions on the wave. The result is a compression of the waveform, as the peak of the sinusoid will propagate faster than the valley, and the wave will gradually transition from a sinusoid into the shape of a sawtooth [4]. This distortion of the waveform means that the fundamental frequency, the one generated at the acoustic source, is no longer the only frequency making up the wave. Instead, higher harmonics of the fundamental frequency are generated as the wave propagates [4]. Because this distortion of the waveform is caused by differences in density at different points on the wave, its severity is dependent on the amplitude of the acoustic wave. The larger the amplitude, the more the wave is distorted [4]. As higher frequencies also attenuate at a higher rate, the distortion of the wave leads to increased attenuation.

2.2 Equipment and setup

All measurements were made in an ultrasound lab, in collaboration with Magnus Cinthio's group at the Department of Biomedical Engineering, Lund University. The output from an ultrasound transducer (model L7-4 manufactured by Philips Ultrasound) frequently used within the group was studied in two different settings: while propagating unhindered through water, and while propagating through water after having passed through a piece of skull bone. The transducer produces

4

sound using an array of 128 piezoelectric elements that can be individually activated. For our measurements the transducer was set to activate 12 elements around the center of the array. The frequency was set to 6 MHz, the powering voltage was 18 V, and the transducer was set to produce unfocused lines, as these are the settings currently used within the group for other measurements. The transducer was connected to an ultrasound machine from VeraSonics (model Vantage 64/32 and configuration Vantage 32 LE) and mounted in a water filled aquarium with sound absorbing panels covering the walls. It was held in place by a clamp and its position remained unchanged throughout the measurements. A 0.5 mm needle hydrophone (SN 3488) from Precision Acoustics, attached to a computer controlled translation stage that allowed for automatic movement in three dimensions, was used to measure the sound. An oscilloscope connected to the hydrophone via a pre-amplifier and DC connector recorded and transferred the signal to the same computer controlling the translation stage.

The skull bone used in the measurements was a piece of bone from an infant cranium. Although the bone was curved, it was placed so that a flat part touched the transducer at the center where sound would be generated. It was held in place by a clamp, and its position was not changed throughout the measurement. The bone was measured to be about 1.5 mm $\pm$ 0.5 mm thick at the position where the ultrasound propagated through.

2.3 Measurements

Two measurements of the ultrasound transducer will be discussed in this thesis. One where the pulse was allowed to propagate through water without hindrance, which from hereon will be called the reference measurement or reference pulse, and one where the pulse was measured after propagating through the skull bone, which from hereon will be called the skull measurement or the skull pulse.

Figure 2 shows a photograph of the transducer and hydrophone set up in the aquarium, with Cartesian coordinate axes drawn for reference. The hydrophone recorded the pressure oscillations over time, and by varying its position in three dimensions the spatial pressure distribution of the ultrasound pulse was studied.
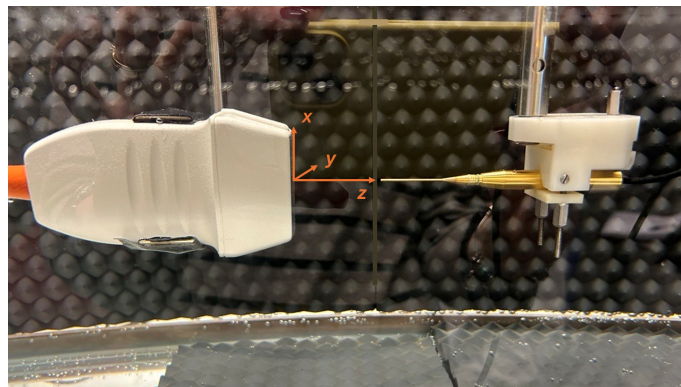

Figure 2: Photograph of the experimental setup including ultrasound transducer and hydrophone facing each other in the water filled aquarium with a Cartesian coordinate system drawn into the image. The z-axis corresponds to the axis of propagation for the ultrasound pulse. The origin is placed in the center of the transducer's element array, from which the pulse would originate.

To see how the pulses changed as they propagated, measurements were made at the following fifteen different distances from the transducer (or fifteen points on the z-axis drawn in Figure 2): 0.5 cm, 1.0 cm, 1.5 cm, 2.0 cm, 2.5 cm, 3.0 cm, 3.5 cm, 4.0 cm, 4.5 cm, 5.0 cm, 6.0 cm, 7.0 cm, 8.0 cm, 9.0 cm and 10.0 cm. At each of these distances the hydrophone was moved to positions specified by a grid of equally spaced points in the xy-plane. The number of points, i.e. the spatial resolution, could be set in the software, but was limited in our measurements by time constraints. As a compromise between spatial range, spatial resolution, and time constraints, two grids were scanned at each of the fifteen z-coordinates:

- One 30×30 mm image with 2.5 mm between each measurement position, from hereon called the *large measurement*

- One 5×5 mm image with 0.5 mm between each measurement position, from hereon called the *small measurement*

The thought behind these combined grids was based on previous similar measurements of the transducer. These previous attempts within the group had shown a Lorentzian looking peak in the pressure distribution transverse to the axis of propagation. However, the full tails of the peaks were not captured by the small images. Our idea was to measure one large image to ensure that the entire range of the peak was covered and one smaller image with higher resolution to capture the central shape of the peak.

The small measurements generated data in the form of 11×11×1000 matrices, whereas the large measurements generated data in the form of 13×13×1000 matrices. The first two dimensions represent the number of measurement points in the xy-plane, 11×11 and 13×13, respectively. The third dimension contains the pressure sampled 1000 times at each spatial position. The temporal resolution is given by the sample rate of the oscilloscope, which was set to 50 MHz, making the duration of each measurement 20 μs and the time interval between two samples 20 ns.

2.4   Results

Figure 3 shows an example of the data recorded by the hydrophone. The voltage from the oscilloscope has been converted to pressure by using the conversion factor 0.465 V/MPa, given by the sensitivity of the hydrophone.

(a) Pressure measured at 1000 time stamps over 20 μs

(b) Pressure measured between 4 and 7 μs, where the pulse is contained.
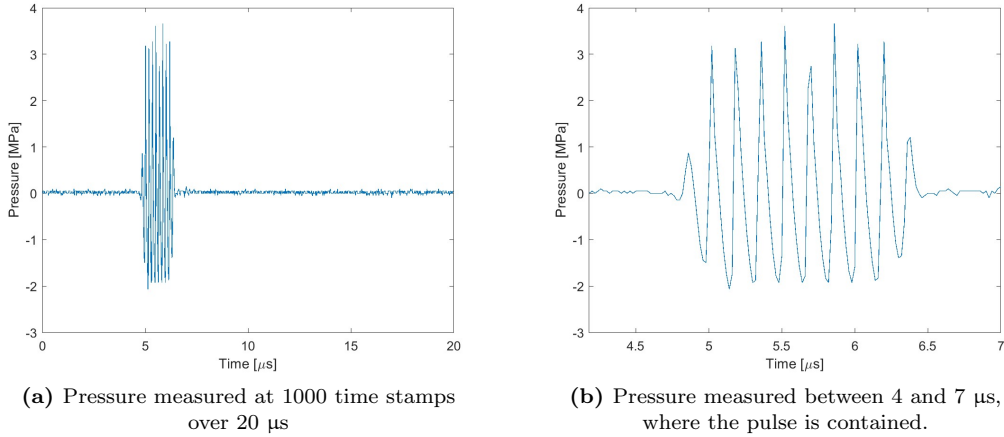
Figure 3: Pressure measured at (x,y,z) = (0,0,3) cm, plotted over time.

2.4.1 Pressure output at different voltages

As previously mentioned, the voltage powering the transducer was set to 18 V. However, the reference pulse was also measured while using other input voltages. The aim was to find what input voltages would produce pressures below the medical safety limit. Such a limit is put on the peak negative pressure from transducers, as negative pressures below a certain value, upheld for too long, cause vaporisation of the sound medium, which causes cell destruction if the medium is tissue. The limit is defined by a mechanical index $\text{MI} = \frac{P_-[\text{MPa}]}{\sqrt{f_{\text{US}}[\text{MHz}]}}$ and if $\text{MI} \leq 1.9$ the ultrasound is considered safe [2]. For a frequency of 6 MHz this would correspond to $P_- \geq -4.65$ MPa. These results confirmed that the 18 V ultrasound pulse was medically safe, and that an increase in voltage, and thereby acoustic amplitude, was possible.

Therefore pulses by input voltages ranging from 12 V to 24 V were studied at the spatial position where the peak negative pressure was found to be the largest (this turned out to be at (x,y,z) ≈ (0,0,2) cm). No voltage above 24 V was used due to limitations of the transducer. The peak negative pressures were calculated as a mean of the oscillation minima in the pulses (like the one shown in Figure 3). The result of these measurements are plotted in Figure 4. As the figure shows, none of the voltages produced peak negative pressures below −4.65 MPa.

Figure 4: Peak negative pressures measured at (x,y,z) = (0,0,2) cm plotted over input voltages to the transducer. All values stay below the medical safety limit at 6 MHz, which is -4.65 MPa
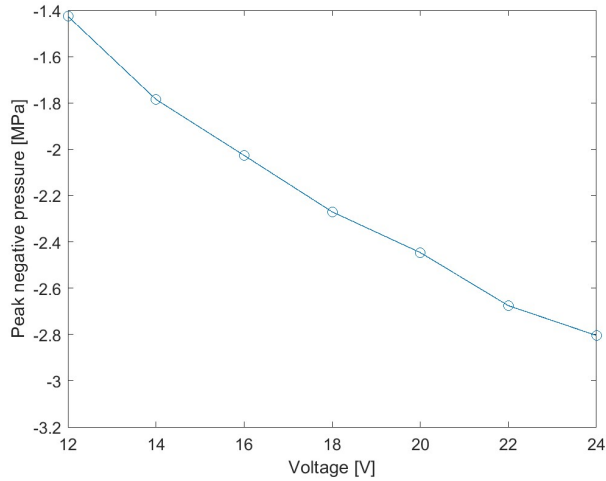
2.4.2 Peak positive pressure

To view how the amplitude of the pulses varied in space, the peak positive pressure was plotted over the xy-plane at each measured position on the z-axis. The peak positive pressure at each point in space was calculated as a mean of the oscillation maxima in the pulses (like the one shown in Figure 3). The result is shown in Figures 5, 6 and 7. The graphs combine the large and small measurements by first linearly interpolating the low resolution data in the large measurements to 0.5 mm resolution, and then replacing the datapoints within the 5×5 mm middle square with the data from the small measurements.

The graphs from the reference measurement show that even though the transducer is set to generate an unfocused line, there is still an axial focus around z = 3.0 cm. At this distance the peak positive pressure distribution shows the thinnest and highest peak, while distances smaller or larger than 3.0 cm show broader and lower peaks. This differs slightly from the peak negative pressure distribution, which was the highest at about z = 2.0 cm. At distances z ≤ 1.5 cm the pulse shape can not be described as a single peak, but as a group of peaks – likely an interference pattern. At larger z however, the distributions seem to show single peaks, with some oscillations in the tails.

The figures also contain graphs from the skull measurement. In comparison with the peaks from the reference measurement, the peaks from the skull measurement are noticeably smaller. On average, they are about 30% the height of the reference peaks, but at the closest distance, 0.5 cm from the transducer, the peak is about 40% of the peak from the reference pulse. The highest peak value is also slightly closer to the transducer compared to the reference data, at z = 2.5 cm. Cross sections of the skull measurement peaks showed diagonal orientations of the peaks, that rotated as the pulse propagated. This indicates that some astigmatism was given to the pulse when it passed through the bone.

(a) 5 mm from transducer

(b) 10 mm from the transducer

(c) 15 mm from the transducer

(d) 20 mm from the transducer

(e) 25 mm from the transducer

(f) 30 mm from the transducer

Figure 5: Peak positive pressure distributions of pulses in the xy-planes, from z = 5 mm to z = 30 mm, calculated by averaging over each pulse's peak positive maxima.

(a) 35 mm from the transducer

(b) 40 mm from the transducer

(c) 45 mm from the transducer

(d) 50 mm from the transducer

(e) 60 mm from the transducer

(f) 70 mm from the transducer

Figure 6: Peak positive pressure distributions of the pulses in the xy-planes, from z = 3.5 cm to z = 7.0 cm, calculated by averaging over each pulse's peak positive maxima.

(a) 80 mm from the transducer

(b) 90 mm from the transducer
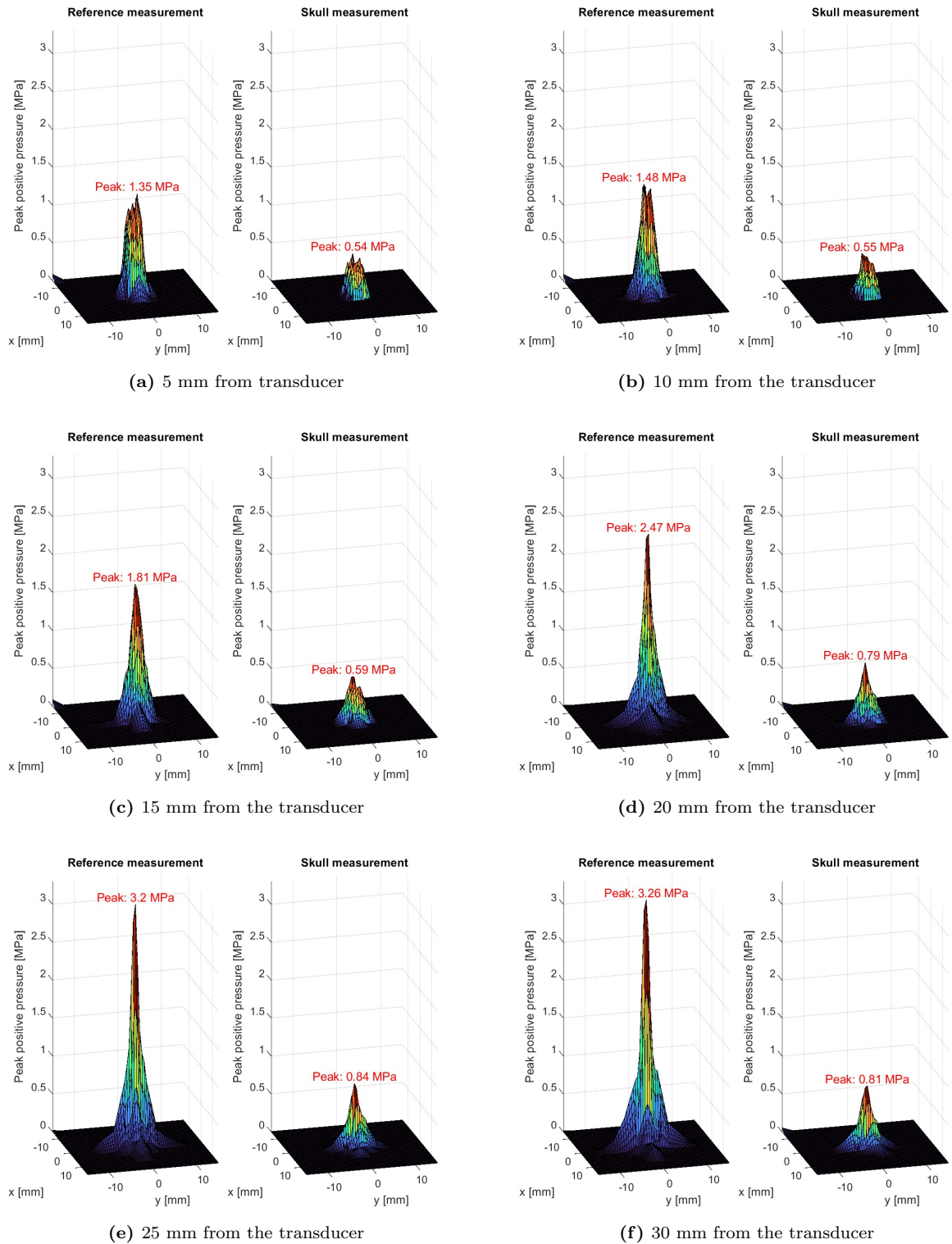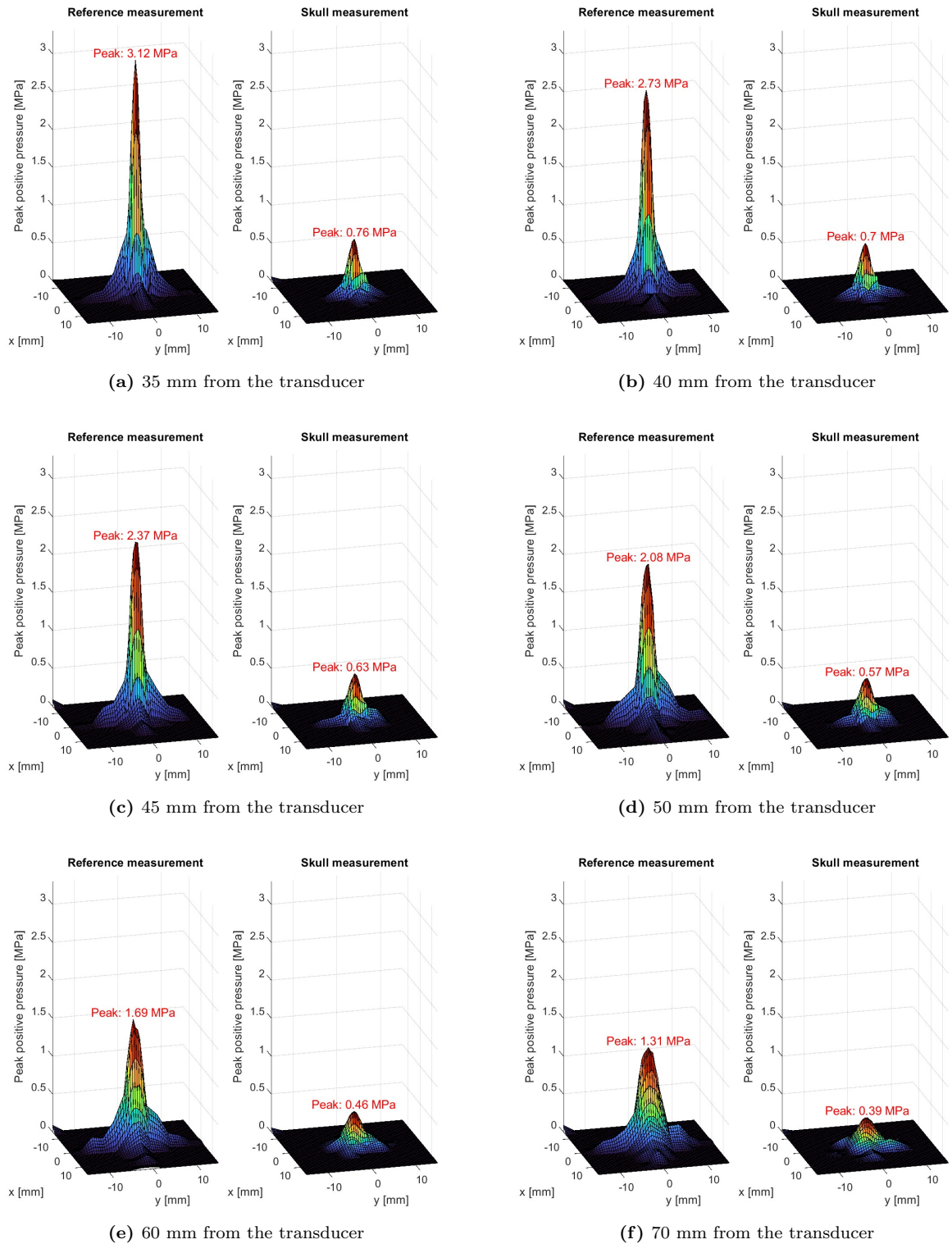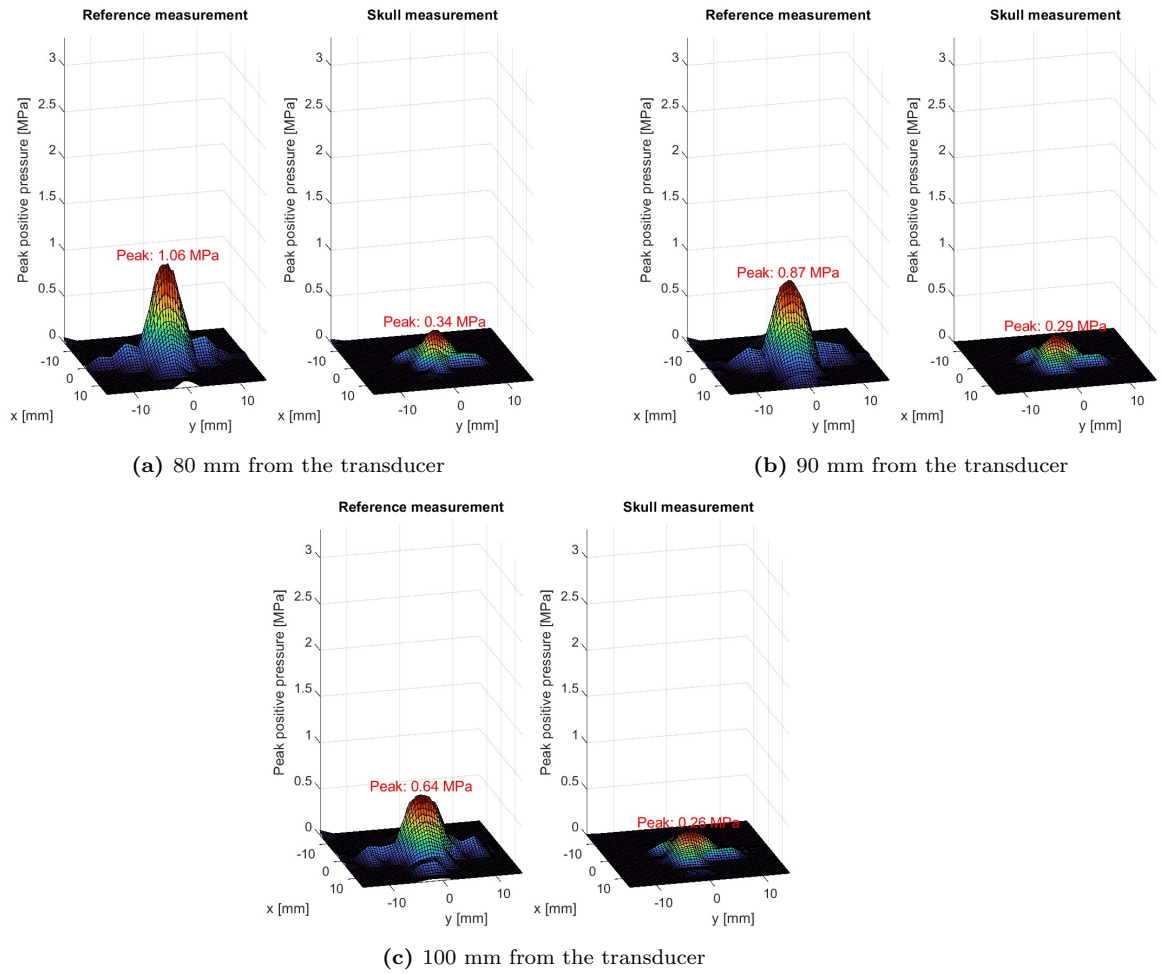
(c) 100 mm from the transducer

Figure 7: Peak positive pressure distributions of the pulses in the xy-planes, from z = 8.0 cm to z = 10.0 cm, calculated by averaging over each pulse's peak positive maxima.

2.4.3 Attenuation of the pulses

To study the attenuation of the pulses as they propagated, the energy at each distance from the transducer was calculated. This was done by combining the large and small measurements without interpolation. The middle 5×5 mm square in the large 30×30 mm data grid was excluded and replaced by the small data. The calculations were made according to Equation 2 [1]:

$$E = \int P(t)\, dt = \int \int_A I(\mathbf{r}, t)\, d\mathbf{r}\, dt = \int \int_A \frac{p^2(\mathbf{r}, t)}{2\rho v}\, d\mathbf{r}\, dt \; . \tag{2}$$

Here P is power, A is the pulse area, t is time, I is the intensity, p is the pressure, ρ is the water density 997 kg/m^3, and v is the speed of sound, which is assumed to be 1480 m/s in the water filled tank. From Equation 2, we calculate the energy $E(z)$ at each distance z from the transducer:

$$E(z) = \Delta t \sum_{k=1}^{1000} (2.5 \text{ mm})^2 \sum_{j=1}^{13} \sum_{i=1}^{13} I_{ijk}^l + \Delta t \sum_{k=1}^{1000} (0.5 \text{ mm})^2 \sum_{j=1}^{11} \sum_{i=1}^{11} I_{ijk}^s \, ,$$

$$I_{ijk}(z) = \frac{p_{ijk}(z)^2}{2\rho v} \, , \tag{3}$$

where p_{ijk} is the pressure at indices i, j, k in the three dimensional matrices we acquired at each distance z from the transducer, s and l denote the small and large measurements respectively, and $\Delta t = 20$ ns is the temporal resolution of the measurements.
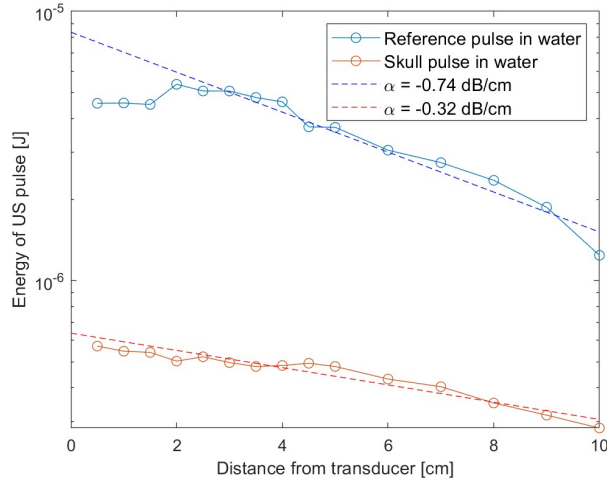
Figure 8: Energy of the reference pulse and skull pulse as they propagate in the z-direction, calculated according to Equation 3. The fitted equations are $E_{\text{reference}} = 8.3640 \times 10^{-6} \times 10^{-0.074z}$ J and $E_{\text{skull}} = 6.3867 \times 10^{-7} \times 10^{-0.032z}$ J, with slopes corresponding to attenuation coefficients 0.74 dB/cm and 0.32 dB/cm in water.

Figure 8 shows the calculated energy of the ultrasound pulse plotted over the z-axis defined in figure 2. Both the reference measurement and the skull measurement are included in the figure, as well as two fits to the data, which will be discussed below. The reference pulse shows a strange increase in energy between $z = 1.5$ cm and $z = 2.0$ cm. It seems as though the measurements at the first three distances have underestimated the energy of the ultrasound pulse – or alternatively as though

the five measurement points between $z = 2.0$ cm and $z = 4.0$ cm have overestimated the pulse energy. By viewing the pressure distributions at distances $z = 0.5-1.5$ cm in Figure 5, we can see that the pulse does not look like one single peak, but many small ones. Although the hydrophone was aligned before the measurements, the alignment was only performed at $z = 3.0$ cm. At this distance the hydrophone was placed so that one of the measurement positions was aligned with the peak positive pressure maximum (see Figure 5f), but this does not ensure that the hydrophone hits all of the smaller peaks shown in Figure 5a-b. Therefore it is likely that the hydrophone did not measure the pressure at the maxima of the closer profiles, resulting in an underestimation of the energy at $z \leq 1.5$ cm. The pressure distributions in Figure 7 also show that at large z, the pulse may not be fully contained within our 30×30 mm measurement range. Therefore there is a risk that the measurements at the largest distances from the transducer also underestimate the energy.

Figure 8 also shows that the energy of the skull pulse seems to be between 10-15% of the energy of the reference pulse. At the closest distance, 0.5 cm from the transducer, the ratio is about 12%. If we assume that the pulse does not attenuate much over 0.5 cm in water, and therefore contains most of its initial energy at this distance, we can estimate that about 82% of the ultrasound energy was lost as it propagated through the bone. We could also make an estimate by seeing what energy the linear fits in Figure 8 assume at $z = 0.15$ cm (which would be the coordinate where the pulse exits the skull bone). In this way, the linear fits would indicate that the energy lost in the skull is about 92%.

As the scale in Figure 8 is logarithmic with base 10, a linear fit to the plots should have a slope corresponding to the acoustic attenuation coefficient of water, according to Equation 1. Fits to the data resulted in the equations

$$E_{\text{reference}} = 8.3640 \times 10^{-6} \times 10^{-0.074z} \text{ J} ,$$
$$E_{\text{skull}} = 6.3867 \times 10^{-7} \times 10^{-0.032z} \text{ J} ,$$

corresponding to water attenuation coefficients of 0.74 dB/cm and 0.32 dB/cm. The attenuation coefficient of water in the skull measurement is here estimated to be about half of the attenuation coefficient in the reference measurement. One possible explanation to this will be mentioned in section 2.4.4.

2.4.4   Nonlinear propagation and frequency contents of the pulse

To study the frequency contents of the pulses, the pressure oscillations like the one shown in Figure 3, were Fourier transformed. At each distance z from the transducer the pressure array from only one position in the xy-plane, namely the one where the peak positive pressure reached its maximum, was Fourier transformed. Figure 9 shows an example of what the Fourier transforms looked like.
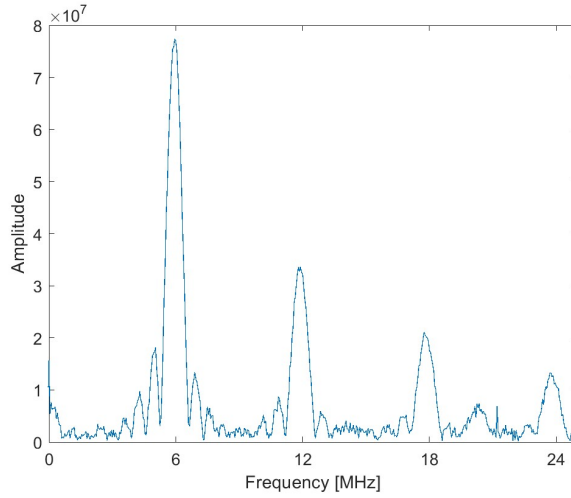
Figure 9: Fourier transform of the ultrasound pulse shown in Figure 3, measured at (x,y,z) = (0,0,3) cm.

The figure shows prominent peaks at 6 MHz, 12 MHz, 18 MHz, and 24 MHz, i.e. at the fundamental frequency and three higher harmonics. As the sampling frequency of the oscilloscope was 50 MHz, the highest frequency detectable was 25 MHz according to Nyquists theorem. Fourier transforms at other distances z showed peaks at the same frequencies, both from the reference measurement and the skull measurement. However, the relative sizes of the peaks differed.

Figure 10a shows the relative amplitudes of the fundamental frequency and the first three higher harmonics in the reference pulse. The sum of the components is normalized to one so that the curves show the relative size of each frequency component. We can see that the 6 MHz component is dominating at the start, constituting about 90% of the pressure amplitude. The share however quickly decreases to about 50% at z = 3.0 cm, where it remains. Something similar can be seen in Figure 10b, which shows the relative amplitudes of the same frequency components in the skull pulse. However, in this pulse, the fundamental frequency starts out at over 90% and does not decrease below about 70%. Both figures clearly show the frequency contents of the pulse changing as the sound propagates through the water. The figures also show that the frequency contents of the skull pulse is different to that of the reference pulse.

14

(a) Reference pulse **(b)** Skull pulse

Figure 10: The relative amplitudes of the frequency contents of the pulses, including the fundamental frequency as well as the first three higher harmonics plotted as the pulse propagates in the z-direction.

The generation of higher harmonics of the sound frequency as the pulse propagates can be explained by the nonlinear propagation of ultrasound, described in section 2.1. We are however unsure of the apparent equilibrium that is shown in both Figures 10a and 10b. As an ultrasound 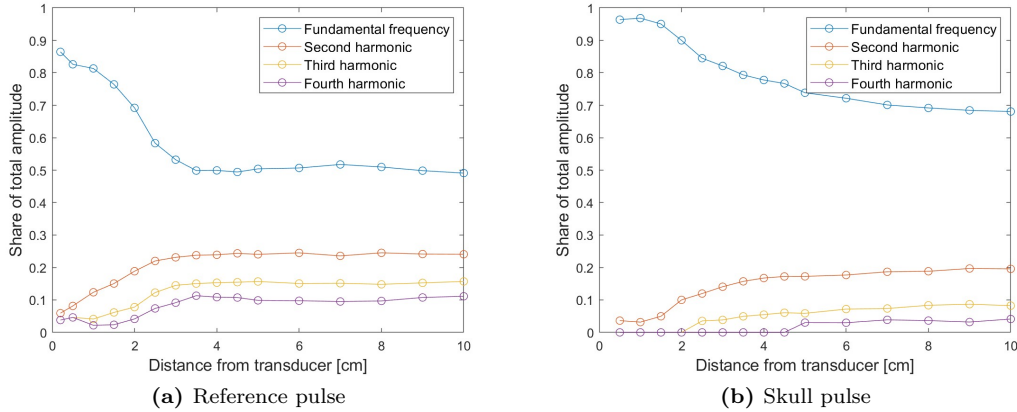wave propagates the generation of higher harmonics should slow down when the amplitude of the pulse attenuates, but the generation seems to stop at around z = 3.0 cm, which is where the pulse has its highest pressure amplitude due to axial focusing. The relationship between amplitude and pulse distortion may however explain the difference between Figure 10a and 10b. The pulse has a smaller amplitude after passing through skull bone as shown in Figures 5-7, which would cause a lesser distortion of the pulse and less harmonic generation.

The differing frequency contents of the pulses may in turn explain the difference between their attenuations in water. Even though both pulses propagate through water, Figure 8 shows the skull pulse being attenuated less. This could be because a larger share of the pulse energy is carried by higher harmonic frequencies in the reference pulse than in the skull pulse, and the attenuation coefficient in water is larger for higher ultrasound frequencies.

2.5   Model fitting

To simulate UOT in the brain we need to know the shape of an ultrasound pulse after passing through the skull bone. Therefore the data from the skull pulse was used to fit a model of the pulse. The fitting can be divided into a temporal part and a spatial part, which will be discussed separately.

For the temporal part of the fitting, the pressure arrays like the one plotted in Figure 3, from one position in the xy-plane at each distance z were Fourier transformed. Once again the position selected was the one with the highest peak positive pressure (see Figures 5-7). As in the previous section, the amplitudes of the fundamental frequency and the three first higher harmonics were found and normalized so that their sum was equal to one. The pulse in the time domain was then

modelled as a sum of five plane waves with the corresponding frequencies:

$$p(t, z) = \sum_{j=1}^{5} a_j(z) \sin[jk_0(vt - z) + \phi_j(z)] , \tag{4}$$

where a_j is the amplitude of frequency component $j \times 6$ MHz, v and k_0 are the ultrasound velocity and wave vector in water at 6 MHz. The phases ϕ_j were determined by fitting the equation to the data. The shape of the pulse envelope was modelled as a supergaussian:

$$G(t) = \exp(-t/\sigma_t)^{12} . \tag{5}$$

The parameter $\sigma_t = 0.74$ μs was determined by fitting Equations 4 and 5 to the data, and represents the characteristic time duration of the pulse. This corresponds to a spatial characteristic along the z-axis of $\sigma_z = v\sigma_t$.

For the spatial part of the fit, the peak positive pressure distributions shown in Figures 5-7 were considered. A Lorentzian peak of the form

$$L(x, y) = \Gamma \times \frac{1}{4(x/\sigma_x(z))^2 + 1} \times \frac{1}{4(y/\sigma_y(z))^2 + 1} , \tag{6}$$

was fitted to the data. The Lorentzian profiles did not capture the shapes of the pulses perfectly as the shapes were irregular after passing through the skull bone. Separate parameters were found for Equations 4-6 at each distance z from the transducer, and are shown in Table 1.

Table 1: Parameters of Equations 4 - 6 at 15 distances z from the transducer, for the ultrasound pulse measured after propagating through a slab of the skull bone.

z [cm]	0.5	1.0	1.5	2.0	2.5	3.0	3.5	4.0	4.5	5.0	6.0	7.0	8.0	9.0	10.0
a_1	0.96	0.97	0.95	0.90	0.84	0.82	0.79	0.78	0.77	0.74	0.72	0.70	0.69	0.68	0.68
a_2	0.04	0.03	0.05	0.1	0.12	0.14	0.16	0.17	0.17	0.17	0.18	0.19	0.19	0.20	0.20
a_3	0	0	0	0	0.04	0.04	0.05	0.05	0.06	0.06	0.07	0.07	0.08	0.09	0.08
a_4	0	0	0	0	0	0	0	0	0	0.03	0.03	0.04	0.04	0.03	0.04
ϕ_1	0	0	0	0	0	0	0	0	0	0	0	0	0	0	0
ϕ_2	0.99	5.80	6.09	5.61	5.58	5.44	5.79	5.88	0.04	5.51	5.15	0.13	6.00	0.16	1.14
ϕ_3	-	-	-	-	4.88	4.60	5.17	5.27	5.77	4.60	4.03	6.01	5.43	6.05	1.32
ϕ_4	-	-	-	-	-	-	-	-	-	3.59	2.76	5.45	4.84	5.50	1.49
σ_x [mm]	3.26	2.97	2.55	1.84	1.73	1.71	1.90	2.09	2.47	2.99	3.60	4.41	4.75	5.81	6.44
σ_y [mm]	3.00	2.99	3.35	2.99	3.14	3.30	3.35	3.57	3.91	4.26	4.94	5.20	5.49	5.92	6.24
Γ [MPa]	0.54	0.56	0.62	0.79	0.84	0.81	0.76	0.70	0.63	0.57	0.47	0.41	0.36	0.32	0.28

2.6 Discussion

The ultrasound measurements provided information on the effect that a layer of skull bone would have on a 6 MHz pulse from the L7-4 transducer by Philips Ultrasound. They also provided a new reference for the characteristics of an ultrasound pulse traveling through water or a water-like medium. However, the shape of the pulse is specific to the constellation of piezoelectric elements generating it. Although Lorentzian approximations of the lateral pressure distributions of the pulse were made, a more accurate analytical description of the reference pulse would likely be a superposition of 12 Fresnel-diffracted waves with sources along the transducer's element array. The oscillations at the tails visible in the reference pulses shown in Figure 7 are likely fringe patterns from interference between the 12 sound waves. The actual shape of the pulse after passing through the skull bone is completely dependent on the random inhomogeneous shapes of the spongy bone contained inside the slab, and can likely not be expressed analytically. Therefore, the exact irregular shape of the pulse after passing through the bone may be considered highly case specific.

However, by looking at Figures 5-7, we can conclude that the pulse shape was not severely distorted by the skull bone. We can also conclude that the peak positive pressure of the pulse at the lateral maximum, immediately after exiting the bone is about 40% of the maximum peak positive pressure that the reference pulse had after propagating the same distance through only water. The results also show that the energy of the pulse immediately after exiting the bone is about 12% of the reference pulse energy after passing the same distance through water. These may be more general results, specific to the ultrasound frequency, initial amplitude, the thickness and composition of the skull bone. Note that the bone used during these measurements was only about 1.5 mm thick, as it was from an infant cranium. Thicker bones from adult skulls would have a larger effect on the ultrasound pulse.

As we did not have much knowledge of the nonlinear nature of ultrasound propagation prior to the measurements, the measured frequency contents of the pulses left us with some questions. Why does the rate of harmonic frequency generation suddenly diminish when the ultrasound pulse is at its highest amplitude? How does brain tissue or other tissues differ from water in this regard? As this affects both the acoustic attenuation coefficient of the medium, and the tagging frequencies that would be generating the signal in UOT imaging, further reading or investigation would be of interest.

Finally, one possibly large source of error should be addressed. The aquarium in which the measurements were conducted was filled with water from a hose in the lab. The water from this hose contained many small microbubbles of air, that gradually grew and attached to equipment during the course of the measurements. Bubbles on the hydrophone and transducer were regularly removed, but any undetected bubbles would have an unpredictable dampening effect on the acoustic signal. Furthermore, the skull bone had an internal layer of spongy bone, containing many small hollow spaces. *In vivo* these spaces would be filled with marrow and blood vessels, and in our measurements they should be filled with water. However, any air bubbles formed inside these spaces would not have been be detected or removed during measurements.

3 Optical properties of tissues in the human head

To simulate propagation of light through the human head, a model of its tissue composition is required. Each tissue should be defined by its own set of optical properties, including a scattering coefficient, an absorption coefficient and an anisotropy coefficient (all of which will be further described in section 3.1). As previous searches through literature found conflicting values for the optical properties of brain matter, the ambition was to compare many different studies to find credible estimates.

This chapter begins with a section defining the optical properties that will be included in the search. After this, section 3.2 describes the different tissues that will be considered in our simulations. Finally, sections 3.2.1 - 3.2.4 contain the findings of our searches regarding the separate tissue types of skin, skull, cerebrospinal fluid, and brain matter, respectively. Note that all coefficients mentioned here are for light with wavelengths of around 800 nm.

3.1 Defining the optical properties

As previously mentioned, light is heavily scattered when propagating through tissue. A photon travelling through vacuum does so with a straight path, but in a medium such as tissue the photon will be elastically scattered by cells, nuclei, and organelles it encounters on its way. Each scattering event results in the photon changing its direction by some angle θ. The rate at which scattering events occur for one photon depends on the content of the tissue and is defined by a wavelength-dependent *scattering coefficient* $\mu_s(\lambda)$ [5]. The unit of this coefficient is m^{-1}, as it describes the average number of scattering events per pathlength travelled by the photon. Between scattering events the photon is assumed to propagate in a straight line. The inverse of the scattering coefficient is the mean free path $l_F(\lambda) = 1/\mu_s(\lambda)$, representing the average pathlength travelled by the photon between scattering events.

Scattering in tissue is not isotropic, which means that the probability distribution over possible angles θ added to the angle of incidence is not uniform. Each tissue has its own probability distribution depending on its contents, but θ is usually quite small. One simple way to describe the distribution is with the Henyey-Greenstein phase function, stated below [5]:

$$p(\theta) = \frac{1}{4\pi} \frac{1 - g(\lambda)^2}{(1 + g(\lambda)^2 - 2g(\lambda)\cos(\theta))^{3/2}} \ , \tag{7}$$

where p is the probability that an angle θ is added to the angle of incidence, and g is the *anisotropy coefficient*. The anisotropy coefficient is a wavelength-dependent parameter that varies between tissue types, and is defined as $g(\lambda) = \langle \cos\theta \rangle$. A high value of g corresponds to more forward scattering and a smaller angle θ, while lower values of g corresponds to more isotropic scattering, and $g = 0$ corresponds to complete isotropy.

Scattering can also be described using the *reduced scattering coefficient*, defined in Equation 8 [5]:

$$\mu'_s(\lambda) = \mu_s(\lambda) \times (1 - g(\lambda)) \ . \tag{8}$$

This coefficient corresponds to the probability of isotropic scattering, after the bias towards forward scattering has been deducted from the original coefficient μ_s.

As light propagates through a medium there is also a probability of absorption by the molecules it encounters. This probability is defined by the wavelength-dependent *absorption coefficient* of the

medium $\mu_a(\lambda)$. The unit of the absorption coefficient is also m^{-1}, as it describes the probability of absorption per pathlength travelled by the photon. The total absorption coefficient of the medium is a sum of the absorption coefficients μ_a^i [m^{-1}M^{-1}] of the N number of molecular constituents of the medium, weighted by their respective concentrations C^i [M]. Equation 9 states this relation.

$$\mu_a(\lambda) = \sum_{i=1}^{N} C^i \mu_a^i(\lambda) \; . \tag{9}$$

The absorption coefficient can be used to define the Beer-Lambert law, which expresses the intensity I of light as a function of its incident intensity I_0 and the optical pathlength x it has propagated through a medium with absorption coefficient μ_a [5].

$$I(x) = I_0 \exp(-\mu_a x) \; . \tag{10}$$

3.2 Comparing estimates of the optical properties found in literature

For our simulations, the model of a human head was restricted to include five tissue types, namely scalp, bone, cerebrospinal fluid, grey matter, and white matter. These five layers are similar to models made by other recent Monte Carlo simulation studies [6, 7, 8, 9]. The scalp layer would include the skin and other tissue layers on top of the cranium. The bone layer would include all layers of skull bone. The layer of cerebrospinal fluid models the layer between the bone and brain, which contains thin strands of connective tissue, in a water based fluid. The layers of grey and white matter represent the corresponding two types of brain tissue.

3.2.1 Scalp

Since the 1980s different theoretical models and experimental studies of the optical properties of skin have been published, resulting in a wide range of estimated scattering and absorption coefficients. A review by Mignon et al. [10] comparing 10 different studies over 30 years found that estimates between studies differed by up to 2 orders of magnitude. The authors evaluate each study by comparing its results to known absorption spectra, scattering properties and approximate concentrations of well known chromophores within the different layers of the skin. The known concentrations and prominent absorption peaks of these chromophores are used to find reference values at different wavelengths, with which they compare the datasets from the studies. In this way a subset of the evaluated studies were selected for credibility. Finally, the optical properties of these studies were used in a set of Monte Carlo simulations of light propagation in human skin, and the simulated diffuse reflectance was compared to *in vivo* measurements of diffuse reflectance from human skin [10].

After these evaluations, two studies that included the 800 nm wavelength and together covered all the sublayers of skin (epidermis, dermis, subcutaneous fat) were recommended as credible sources. Those were two experimental studies by Simpson [11] and Wan [12]. The scattering and absorption coefficients of scalp for our model was based on these two studies, even though both have measured skin from abdomen and breast. Our estimates of both the scattering and absorption coefficients were calculated by averaging the coefficients of each layer, weighted by their thicknesses in the

scalp.

$$\mu = \frac{\mu_{\text{epidermis}} w_{\text{epidermis}} + \mu_{\text{dermis}} w_{\text{dermis}} + \mu_{\text{fat}} w_{\text{fat}}}{w_{\text{epidermis}} + w_{\text{dermis}} + w_{\text{fat}}} ,$$

$$\mu_a = \frac{16 \times 0.05 + 0.13 \times 0.3 + 0.084 \times 0.6}{0.05 + 0.3 + 0.6} \text{ cm}^{-1} \approx 0.9 \text{ cm}^{-1} , \tag{11}$$

$$\mu'_s = \frac{20 \times 0.05 + 19 \times 0.3 + 11 \times 0.6}{0.05 + 0.3 + 0.6} \text{ cm}^{-1} \approx 17 \text{ cm}^{-1} .$$

Table 2 shows the layers, their respective optical properties and the widths that were used in our calculations.

Table 2: Thicknesses and optical properties of three layers of skin, used to model the scalp.

Layer	w [mm]	μ'_s [cm^{-1}]	μ_a [cm^{-1}]
Epidermis	0.5	20	16
Dermis	3 [13]	19	0.13
Subcutaneous fat	6 [13]	11	0.084

Between these two studies, only the paper by Simpson et al. [11] mentioned the anisotropy coefficient g. In Monte Carlo simulations used to estimate the scattering and absorption coefficient from experimental reflectance and transmittance spectra, the anisotropy coefficient was assumed to be $g = 0.9$ in all layers of skin. Therefore, we will also use this assumption.

3.2.2 Bone

For the optical properties of skull bone, a smaller set of studies were found, including two *in vivo* and two *in vitro* studies. For our purposes all measurements performed on animal craniums were ignored and only studies with human skull bone were considered. The *in vivo* studies included one measurement performed during a craniotomy [14] and one non-invasive time of flight measurement using light detectors placed on the forehead [15]. The studies estimated the reduced scattering coefficient of skull bone to be $\mu'_s = 9$ cm^{-1} and 10 cm^{-1}, respectively. In contrast, the two *in vitro* studies of skull bone including one integrating sphere measurement [16] and one using a CCD camera [17] resulted in the considerable higher estimates $\mu'_s = 19$ and 39 cm^{-1}, respectively.

In one of the *in vitro* studies, Bashkatov et al. speculated that their higher estimate was due to the postmortem sample being rinsed off and placed in saline prior to measurements, as saline has a slightly lower refractive index than the interstitial fluid that would surround the bone in *in vivo* conditions. The lower refractive index would lead to larger differences in refractive index between bone and fluid, and therefore a higher scattering coefficient [16]. In the other *in vitro* paper, the postmortem sample was stored in formalin and used a method for determining the coefficient that was not found in any other study considered during this literature search.

The absorption coefficient values were more consistent across the four studies, ranging from 0.10 cm^{-1} [17] to 0.22 cm^{-1} [14].

It is difficult to evaluate which results are more credible. One of the *in vivo* papers only contains one single measurement performed on an 8 year old child, but is the only *in vivo* study that

measures the skull bone directly without a barrier of other tissues between the probe and sample [14]. The other *in vivo* study has a good sample size (n=30) and agrees more with the first *in vivo* paper than with the *in vitro* estimates. However, it does not distinguish between different tissue types inside the head, and only specifies the estimated scattering coefficient as a function of depth from the surface of the scalp. Due to the uncertainty, both coefficients were calculated from an average of all four studies, weighted by their sample sizes, making the absorption coefficient 0.12 cm^{-1} and the scattering coefficient 19 cm^{-1}.

As for the anisotropy coefficient g, it is only mentioned in Ref. [17] and Ref. [16], in both cases as a mere assumption. We set the anisotropy coefficient of skull bone to $g = 0.8$, which reflects the assumption made in Ref. [17].

3.2.3 Cerebrospinal fluid

To the best of the author's knowledge there are no experimental measurements of the optical properties of cerebrospinal fluid (CSF). In fact, among the papers attempting to model the human head for Monte Carlo simulations there are examples of models both including and excluding the CSF. However, the effect of including a CSF layer in the model of a human head for Monte Carlo simulations has been studied [18, 19]. Both referenced studies compare the simulated mean optical pathlength in the head to equivalent *in vivo* measurements of the mean optical pathlength. The mean optical pathlength in this context is considered to be the pathlength propagated by the light inside the head, from the source to the detector, averaged over all detected photons. When comparing experimental to simulated data, both studies found a clear improvement in accuracy when a CSF layer was included in the head model. While some simulation papers consider the CSF a non-scattering layer, the investigations in both papers conclude that a better accuracy is achieved with a non-zero scattering coefficient. The optimal range was found to be between $\mu'_s = 1.6$ and 3.2 cm^{-1}. The CSF layer is however usually considered to be transparent, i.e. non-absorbing in the NIR wavelength range.

Considering the results from these studies, the CSF layer in our model is given a scattering coefficient $\mu_s = 2$ cm^{-1}, and is considered to be non-absorbing.

3.2.4 Brain matter

Grey and white matter are outer and inner layers of brain tissue respectively, and contain two different anatomical components of the neuron. Specifically, the neuron cell bodies are contained in the grey matter, while the long cable-like strands known as the axons attached to the cell bodies, are contained in the white matter. The axons transfer electrical signals between neurons, and are surrounded by sheaths of a lipid-rich substance called myelin, which isolates the electric signals from their surroundings. Myelin is mentioned as this substance has been shown to be a large cause of light scattering in the brain, particularly in the white matter where it resides. For example, a recent study found a strong correlation between myelin content and the scattering coefficient of brain tissue samples [20].

Our model of the head includes white matter and grey matter as two separate layers, which means that they can be given separate optical properties. This reflects measurements in most studies we found, that determine their optical properties separately. Much like the optical properties of skin, the estimates differ widely between studies. For our search, studies were selected as follows:

21

- All animal studies were excluded. Only studies with human brain matter were considered.

- All studies that do not differentiate between the scattering and absorption coefficient but instead bundle them together as an attenuation coefficient were excluded.

- All studies that did not differentiate between different types of tissue were excluded, e.g. studies that measured the optical properties of "the forehead".

- Studies that used the Kubelka-Munk method for numerical derivation of the optical properties from data were excluded, as this method assumes isotropic scattering, which is inappropriate for tissue optics, as described in section 3.1.

- However, studies that assumed anisotropy coefficients without measuring, or did not consider them at all and only found the reduced scattering (without the actual scattering coefficient) were included, as this was the case with a majority of the papers found.

As models of both the adult head and the infant head were to be included in our simulations, both studies performed on infant and adult brain matter were considered. Infant and adult studies were however separated, as they consistently gave different estimates of the scattering coefficient in white matter. The reason for this difference will be explored below.

Anisotropy coefficient

Only two studies attempted to measure the anisotropy coefficient g, one by Zee et al. using goniometry [21]) and one by Yaroslavsky et al. using collimated and total transmission spectra from an integrating sphere [22]). From adult brain samples Zee et al. measured $g = 0.85$ for white matter and $g = 0.97$ for grey matter, while Yaroslavsky et al. measured $g = 0.87$ and $g = 0.9$, respectively. As the study by Yaroslavsky et al. had a larger sample size, the grey and white matter values for g in our simulations were taken from their results.

Reduced scattering coefficient

The studies considered for the optical properties in brain matter can be divided into *in vitro* and *in vivo* studies. All *in vitro* studies except the one by Zee et al. [21] only used adult brain samples. The *in vitro* studies examined either postmortem or surgical excision samples and usually obtained larger scattering values, particularly for white matter. They all use an integrating sphere setup for measurements. Two main error sources of this technique have been described by Gebhard et al. [23]. If the sample is not large enough to completely seal the exit and or entrance port, light may escape without being detected, leading to an overestimated absorption coefficient. Furthermore, if the sample is too large and must be compressed to fit in the port, the increased density of the sample will also alter the optical properties and both the scattering and absorption coefficients will be overestimated. The other error sources for this group of measurements are the common ones related to *in vitro* studies of tissue. The tissue has usually been either frozen or contained in saline or formaldehyde during the wait for before measurements. Temperature changes, blood drainage, fluid replacement and mitochondrial swelling, which is associated with death of an organism, are all factors that would affect the optical properties [14, 15].

Three studies with small sample sizes (n = 1,2,2) have significantly larger estimates for the reduced scattering coefficients of both the grey and white matter, compared to other studies. These include papers by Zee et al. with $\mu'_s = 24$ cm^{-1} and 84 cm^{-1} [21], Shapey et al. with $\mu'_s = 25$ cm^{-1} and 89 cm^{-1} [24], and Honda et al. with $\mu'_s = 18$ cm^{-1} and 75 cm^{-1} [25], for grey and white matter respectively (see Table 3).

Table 3: Studies with adult subjects and their scattering coefficients.

Study	White matter μ'_s [cm^{-1}]	Grey matter μ'_s [cm^{-1}]	Sample size	*in vivo/in vitro*
Zee [21]	84	24	n = 2	*in vitro*
Gebhart [23]	42	8	n = 20	*in vitro*
Shapey [24]	89	25	n = 1	*in vitro*
Honda [25]	75	18	n = 2	*in vitro*
Yaroslavsky [22]	48	7	n = 7	*in vitro*
Bevilacqua [14]	9.8	-	n = 2	*in vivo*
Li [26]	26	15	n = 19	*in vivo*

Table 4: Studies with infant subjects and their scattering coefficients.

Study	μ'_s [cm^{-1}]	Sample size	*in vivo/in vitro*
Zhao [27]	9	n = 23	*in vivo*
Ijichi [28]	6	n = 22	*in vivo*
Arri [29]	4	n = 53	*in vivo*
Spinelli [30]	5	n = 33	*in vivo*

On the other hand, two *in vitro* studies were found with slightly larger sample sizes (n = 7,20) that estimated smaller values for both the grey and white matter scattering coefficients. These include one study by Yaroslavsky et al. [22] where both the anisotropy coefficient and reduced scattering coefficients of 7 cadavers were measured, and one study by Gebhart et al. [23] where the diffuse reflectance and transmission spectra (collected by an integrating sphere) from 20 samples were used to estimate a reduced scattering coefficient. In the study by Gebhart et al., the estimated coefficients were also used to find diffuse reflectance spectra from brain matter with Monte Carlo simulations, and the results were compared to *in vivo* measurements of diffuse reflectance spectra from open craniotomies. Yaroslavsky et al. found the reduced scattering coefficient to be $\mu'_s = 7$ cm^{-1} and 48 cm^{-1}, while Gebhart et al. estimated $\mu'_s = 8$ cm^{-1} and 42 cm^{-1} for grey and white matter, respectively (see Table 3). The larger sample sizes, validation by the *in vivo* spectra, and the fact that these two studies found similar estimates make them seem the most credible out of the *in vitro* bunch. The authors of papers [25] with results conflicting with the study by Gebhart et al. have commented on the fact that the samples were frozen in wait for measurements, and even though the study concluded that this did not have a noticeable effect on tissue (by comparing different samples) [23] other studies have found that snap freezing soft tissue may alter its reduced scattering coefficient (decrease by 19%) [31]. However, samples in the study by Yaroslavsky et al. were kept in formalin, in fridge temperatures for less than 48 hours before measurements were performed, and resulted in similar scattering coefficients [22].

Nevertheless, these results should still be compared to *in vivo* estimates of the scattering coefficients. Most *in vivo* studies found in our search included only infant subjects, with the exception of two studies that will be discussed below. In one previously mentioned study by Bevilacqua et al., measurements were performed on the tissue of an 8-year-old child undergoing brain surgery [14]. The measurement resulted in a much smaller estimate of the white matter reduced scatter-

ing coefficient, $\mu'_s = 9.8$ cm^{-1}, than those previously mentioned. The coefficient for grey matter was not measured. Although the conditions of the measurement were *in vivo*, there are some circumstances that may inhibit the generalizability of the results. While the rest of the studies had conducted measurements of the cerebral cortex, this sample was retrieved from the cerebellum. The cerebellum reduced scattering coefficient has been estimated to be about half as large as the cerebrum white matter coefficient [22]. The sample size was limited to one single child with a glioma tumor. Glioma tumors are commonly treated with radiotherapy which is a demylienating procedure. In addition, glioma tumors themselves have been found to cause local demylienation [32] [33]. As the white matter examined was located in the tumor bed, it is possible that its myelin content and therefore its scattering properties were not comparable to those of a healthy brain. The second *in vivo* study on adult brains is one where samples were excised during surgery and used for measurement less than an hour later [26]. Technically this must be classified as *ex vivo*. In this study samples from 19 individuals were retrieved and a small probe-detector pair performed diffuse reflectance spectroscopy. The results were $\mu'_s = 15$ cm^{-1} and 26 cm^{-1} for grey and white matter, respectively, which differs a bit from the selected *in vitro* studies, but not as much as the estimate by Bevilacqua et al. [14] (see Table 3).

As for the *in vivo* infant studies, they included non-invasive time- or frequency domain near infrared spectroscopy (NIRS) measurements performed with a light source-detector pair placed on the surface of the subjects' scalps. The wavelengths used ranged from 780-830 nm, and the separation distance between source and detector differed somewhat between the studies. In these papers no distinction was made between grey and white matter, and only one scattering coefficient was given. The results ranged from about 4 cm^{-1} to 9 cm^{-1} (see Table 4), which is noticeably smaller than all the adult estimates. The sample sizes of these studies were also generally larger, with the largest one including 53 subjects [29]. Although the *in vivo* infant studies seem to give different results from the adult studies, they did not disagree with the one *in vitro* measurement performed on a sample from a term infant [21]. This study estimated the scattering coefficient for grey matter to be 5 cm^{-1} and for white matter to be 10 cm^{-1}.

The reason behind the different scattering coefficient estimates for infant and adult brain matter could be the difference in experimental methods. NIRS performed on a human head may not penetrate deep enough to provide information about the white matter. The scattering coefficients from the *in vivo* infant studies do agree more with those of the grey matter from the adult studies. However, the study by Zee et al. did find a large difference between the infant and the adult samples [21]. One other explanation could be the difference in myelin content in the adult brain compared to the infant brain. It is well established that myelination of the infant brain takes place within the first 1-2 years after birth [34], and as previously mentioned, a high correlation has been found between the scattering coefficient and myelin content in brain samples [20].

Considering the large differences, separate scattering coefficients were assigned to the white matter of the infant model and the adult model. For the adult brain matter, three studies were chosen as the most credible due to their larger sample sizes and relatively consistent results. Those were the *in vivo* study with 19 subjects [26], the *in vitro* study by Gebhart et al. with 20 samples [23], and the *in vitro* study by Yaroslavsky et al. with 7 samples [22]. Averaging the reduced scattering coefficients from each study, weighted by their sample sizes gave the estimates $\mu'_s = 36$ cm^{-1} for white matter and $\mu'_s = 11$ cm^{-1} for grey matter. The infant grey matter was assigned the same reduced scattering coefficient as the adult grey matter, however the white matter was given the significantly lower value $\mu'_s = 10$ cm^{-1} due to the assumed difference in myelin content, and the apparent differences in measurement based estimates.

Absorption coefficient

The same papers mentioned in the previous section all provided estimates of the absorption coefficient of grey and white matter. The estimates varied greatly, by up to two orders of magnitude, specifically among the *in vitro* studies (see Table 5). The values ranged from $\mu_a = 0.01$ cm^{-1} to 0.96 cm^{-1}, and there was even inconsistencies in which absorption coefficient between that of white matter and that of grey matter was the largest.

On the other hand, the *in vivo* studies all found values of around $\mu_a = 0.1$-0.3 cm^{-1} (see Table 6). The difference between results in *in vivo* and *in vitro* studies could be because most of the *in vivo* studies only included infant subjects. It could also be because of the previously mentioned known error sources associated with integrating sphere measurements, which could cause overestimation of the absorption coefficient, or the other common error sources associated with *in vitro* studies of tissue, i.e. sample handling and inevitable postmortem changes.

Table 5: Studies with adult subjects and their absorption coefficients.

Study	White matter μ_a [cm^{-1}]	Grey matter μ_a [cm^{-1}]	Sample size	*in vivo/in vitro*
Bevilacqua [14]	0.13	-	n = 2	*in vivo*
Honda [25]	0.43	0.96	n = 2	*ex vivo*
Zee [21]	0.01	0.32	n = 2	*in vitro*
Yaroslavsky [22]	0.92	0.23	n = 7	*in vitro*
Gebhart [23]	0.62	0.51	n = 20	*in vitro*
Shapey [24]	0.33	0.74	n = 1	*in vitro*

Table 6: Studies with infant subjects and their absorption coefficients.

Study	μ_a [cm^{-1}]	Sample size	*in vivo/in vitro*
Zhao [27]	0.078	n = 23	*in vivo*
Ijichi [28]	0.13	n = 22	*in vivo*
Arri [29]	0.11	n = 53	*in vivo*
Spinelli [30]	0.31	n = 33	*in vivo*

However, for this optical property, a separate group of papers were also considered. These were three *in vivo* studies where oxygenation and haemoglobin concentration of brain tissue was measured using non-invasive time- or frequency domain NIRS [35] [36] [37]. These were interesting as the haemoglobin concentrations were calculated using Equation 9, which requires knowledge of the absorption coefficients of the near infrared absorbing chromophores in brain tissue. In all three studies the participants were children or adults, i.e. not infants, and though each study attempts to compare oxygenation and haemoglobin contents between different groups, they all include healthy control groups with sample sizes of 15-20 subjects. The studies assume that the only relevant chromophores in brain tissue in the NIRS frequency range are water, oxygenated haemoglobin and deoxygenated haemoglobin. They further assume about 80% water volume, and find mean total haemoglobin concentrations of their control groups to be 70 μM [36], 58 μM [35], and 50 μM [37], respectively.

As the absorption spectra of haemoglobin and water are known, and as oxygenated and de-oxygenated haemoglobin have the same absorption coefficient at 800 nm, we can make an estimate of the brain tissue absorption coefficient from the total concentrations mentioned above. As haemoglobin has a coefficient of $\mu_a = 0.001879$ cm^{-1}/μM [38] and water a coefficient of $\mu_a = 0.02$ cm^{-1}/volume fraction [39], the estimated absorption coefficient of brain tissue would be about $\mu_a = 0.13$ cm^{-1} if the haemoglobin concentration was assumed to be 60 μM, according to Equation 9. If the concentrations were instead 40 or 80 μM (this range is taken from the error bars of the three studies), the absorption coefficient would be $\mu_a = 0.09$ cm^{-1} or $\mu_a = 0.16$ cm^{-1}, respectively. All three of these values agree very well with the *in vivo* estimates of the absorption coefficient for brain tissue from the non invasive infant studies (see Table 6), as well as the estimate from the *in vivo* open-surgery study by Bevilaqua et al. performed on a child (see Table 5). Furthermore, the *in vivo* studies in Table 6 also estimate haemoglobin concentrations in their infant subjects' brains to be within the 40-80 μM range, except for the study by Spinelli et al., that found the concentration to be noteably larger, about double this value.

We chose to favor these *in vivo* estimates of the absorption coefficient, rather than the much larger integrated sphere estimates. The absorption coefficient for both grey and white matter is therefore set to $\mu_a = 0.13$ cm^{-1}.

4 Simulating light propagation without ultrasound interaction

To model UOT inside a human head and estimate the size of the signal, a set of simulations were run in MATLAB. The simulations can be divided into two main parts. First, the light propagation was simulated through the sequential Monte Carlo model, described in [2]. As any other Monte Carlo method the simulation is based on repeated random sampling from pre-defined probability distributions, so that statistical conclusions can be drawn from the accumulated result of many samples. In this case, photon paths are sampled repeatedly through a volume representing a human head, to accumulate statistically accurate results of the light propagation in a real head. The second part of the simulation used these paths together with a model of an ultrasound pulse to simulate tagging of the photons.

This chapter concerns the first part of the simulations, that is the simulation of light propagation. A basic description of how the algorithm works is given below in section 4.1, but further details can be found in Ref. [2]. As the Quantum Information group at Lund University currently works with 794 and 689 nm light for UOT, the photons in our simulations were assumed to have wavelengths of about 800 nm. For the simulation of light propagation, this just means that optical properties at 800 nm were chosen, as discussed in chapter 3.

4.1 Description of the algorithm

The simulation takes place inside a *simulation volume*, which is divided into smaller voxels. The voxels are grouped into different domains, representing the tissue types in the simulation volume. Each domain is assigned its own scattering coefficient, absorption coefficient and anisotropy coefficient, all of which have previously been defined in section 3.1. The refractive index can also be specified, but in our simulation a constant refractive index of $n = 1.3$ was set in all domains. Somewhere on the borders of the volume an enclosed area is placed, from which the photons can be initialised. This area is considered the *light source*. Likewise an area defined as the *detector* is placed somewhere on a border of the simulation volume. If the photons enter this area as they propagate, their paths cease to be simulated and they are considered detected. The simulation consists of repeated sampling of paths inside the volume, starting at the light source. Each path is determined in the following way:

1. The photon takes a "step" from its current position, in its current direction (the initial direction is predefined, and the initial position is somewhere in the light source area). This corresponds to a straight line from its current position, in the current direction, being added to the path. The length of the step is sampled from a probability distribution given by the scattering coefficient μ_s:

$$s = \frac{-\ln(\xi)}{\mu_s} \, ,$$

where ξ is a uniform distribution in the interval $]0,1]$. This makes s a number between 0 and infinity, with an average and standard deviation equal to the mean free pathlength $1/\mu_s$ in the medium.

2. A new direction is sampled using the anisotropy coefficient g, through the Henyey Greenstein function defined in Equation 7. In spherical coordinates $[s, \theta, \phi]$, the new angle θ is determined by performing an inverse transform of the cumulative distribution function, as described Ref.

27

[40]. This results in an equation where $\cos(\theta)$ is determined by sampling from:

$$\cos(\theta) = \frac{1}{2g}\left(1 + g^2 - \left(\frac{1-g^2}{1-g+2g\xi}\right)^2\right) \, ,$$

where ξ is a uniform distribution between 0 and 1. In spherical coordinates $[s, \theta, \phi]$, the angle ϕ is simply sampled from a uniform distribution between 0 and 2π.

3. Step 1 and 2 are repeated until the path either enters the detector area or exits the simulation volume without having entered the detector. In both cases the propagation stops, but the path is only saved in the former case.

One by one new paths are calculated until a set number `num_paths` have been saved (i.e. until a set number of photons have been detected). Whenever a path enters a new voxel the optical parameters are updated according to which domain the voxel belongs. No reflection occcurs at internal borders between tissue layers, or at the external borders, as the same refractive index is set everywhere.

The paths simulated represent how photons would propagate within the volume if they were never absorbed, but as described in section 3.1, there is a probability of absorption as light propagates through tissue. The absorption is accounted for by weighting each path using considering Beer-Lamberts law (defined in Equation 10). From the simulated paths a matrix $\mathbf{D} = (d_{i,j})$ of size `num_paths` $\times$ `nbr_voxels` is created, where each index i,j represents the size of the pathlength that photon i spent inside voxel j. The weight of each path can then be calculated as:

$$\mathbf{W} = \exp(-\mathbf{D} \cdot \mu_a) \, , \tag{12}$$

where μ_a is the `nbr_voxels` $\times$ 1 sized matrix assigning an absorption coefficient to each voxel in the volume and $\mathbf{W}$ is a matrix of size `num_paths` $\times$ 1 containing the weight of each path.

4.2   Configuration and parameters of the simulations

As previously mentioned our simulations took place in two different volumes – one representing a part of an adult head and the other a part of an infant head. Both simulation volumes were cuboids of sizes $9\times9\times3.6$ cm^3, divided into voxels of sizes $0.12\times0.12\times0.12$ cm^3, which corresponds to $75\times75\times30$ voxels in the x- y- and z-direction, respectively. An illustration of the simulation volumes is shown in Figure 11. The domains separating the volume into tissue types are five slabs stacked on top of each other, representing the five tissue layers scalp, skull, cerebrospinal fluid, grey matter and white matter. The optical parameters of each layer were chosen according to the selections in chapter 3, and are listed in Tables 7 and 8. The thickness of each layer was chosen so that the volume would represent a human forehead. As the tables show, the only differences between the adult and infant simulation volumes are the thicknesses of the tissue layers, and the scattering coefficient of white matter.
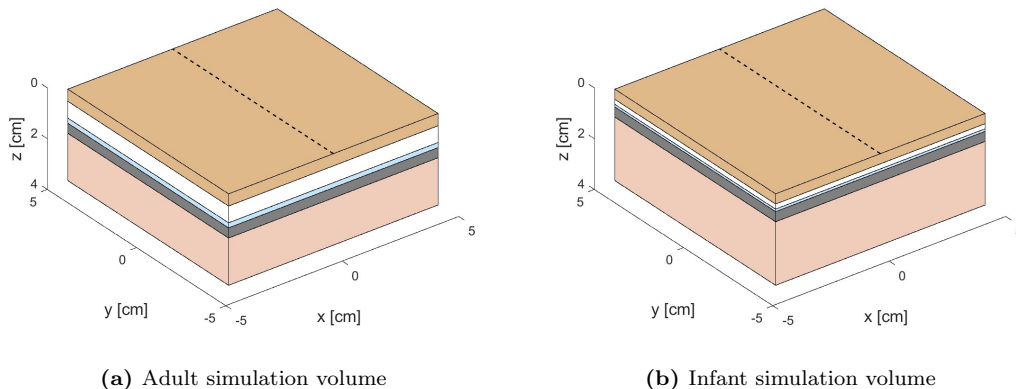
(a) Adult simulation volume

(b) Infant simulation volume

Figure 11: Schematic illustration of the adult and infant simulation volumes. The layers from top to bottom represent the following tissues: scalp, skull, cerebrospinal fluid, grey matter, and white matter. The light source and detector are both placed on the dashed line on the surface of the scalp, with an equal distance $L/2$ to the origin.

For both simulation volumes the light source is a circle with 5 mm radius, located at the top plane of the volume (representing the outer surface of the scalp). The photons can be initialised at any position inside the light source area with equal probability, meaning that the "intensity profile" of the source is uniform. The initial direction of the photons is always straight down in the z-direction.

The detector in our simulations is also a circle with 5 mm radius, placed at the top plane of the simulation volume. As the light source and detector are placed on the same surface, our simulation will show propagation of reflected light. Both the detector and light source are placed on the y-axis (the dashed line in Figure 11), with equal distances $L/2$ to the origin. The distance L is called the light source-detector separation, and is varied from 0.5 cm to 5 cm in increments of 0.5 cm. At each separation L a new simulation is run, which corresponds to a total of ten simulations in each of the two volumes.

The simulations are run until 50 000 paths have been saved, making `num_paths` = 50 000. This was the highest number that our time constraints allowed. It corresponds to much larger numbers of initiated paths Z (i.e. the total number of paths simulated, including those that never reach the detector, and thus are not saved), which ranged from $Z = 10^6$ for the smallest L to $Z = 10^8$ for the largest L. The latter is comparable to the number of initiated photons used in other papers on Monte Carlo simulations of light propagation in head tissue [6, 41, 42, 43, 44].

Table 7: Adult simulation volume: Optical properties assigned to each tissue layer, as well as the thickness of each tissue layer.

Layer	μ_a [cm^{-1}]	μ_s' [cm^{-1}]	g	Thickness [mm]
Scalp	0.90	17	0.9	4.8 [45]
Skull	0.12	19	0.8	6.6 [46]
Cerebrospinal fluid	0	2	0.9	2.0 [19] [18]
Grey matter	0.13	11	0.9	4.0 [47]
White matter	0.13	36	0.87	-

Table 8: Infant simulation volume: Optical properties assigned to each tissue layer, as well as the thickness of each tissue layer.

Layer	μ_a [cm^{-1}]	μ_s' [cm^{-1}]	g	Thickness [mm]
Scalp	0.90	17	0.9	4.0 [48]
Skull	0.12	19	0.8	2.0 [49]
Cerebrospinal fluid	0	2	0.9	1.0
Grey matter	0.13	11	0.9	4.0
White matter	0.13	10	0.87	-

4.3 Evaluation of the size of our simulation volume

The shape of the simulation volume is a simple cuboid, representing a finite volume of the larger head. The cuboid shape may be realistically contained within a human head when the area is sufficiently small, but as the width of the volume increases a flat surface may not be realistic as it would ignore the curvature of the head. A surface area of 9×9 cm^2 seems too big to be modelled as flat on the adult human head, and even more so on the infant head. However curvature has in no way been accounted for in this work.

The purpose of the large size is to avoid too many photons escaping through the borders of the simulation volume and never being detected, when they in reality might have returned back to the detector. This is particularly relevant in the simulations where L is large, as the photon paths would be initiated close to the side-borders. If photons escape through the top surface, i.e. the scalp surface, this would reflect reality as they can be considered lost. However, if they escape through any other boundary they are technically only lost due to the limitation of the simulation volume, as the real photons would still be propagating inside the head with a possibility to return. Of course the simulation volume can not be increased to an infinite size, as it must not be made larger than the head it simulates.

To investigate the size of the error caused by the escaped photons, one simulation in a volume of a slightly larger width (10.2×10.2×3.6 cm^3) was run, with the largest light source-detector separation $L = 5$ cm, and the result was compared to that of the 9×9×3.6 cm^3 simulation with the same L. For this investigation, the total pathlength travelled in each voxel ($\mathbf{Q} = \sum_{i=1}^{50000} d_{i,j}$, where $d_{i,j}$ is the element at index i, j in matrix $\mathbf{D}$) was used to compare the two simulations. As the light source and detector are placed on the y-axis, the paths will be most dense around the x = 0 plane. The x = 0 plane is therefore mostly imaged and discussed in the results, and thus a slab around this plane with a thickness of about 1 cm (9.6 mm, or 8 voxels) was considered for the comparison. This slab contained 18 000 voxels in the small (9×9×3.6 cm^3) simulation volume, and only voxels

within this region were considered in the large ($10.2 \times 10.2 \times 3.6$ cm^3) volume. That is to say, the outer layer of the large volume was not included in the comparison, as the small volume did not contain these voxels.

We expect to see a variation in error size over different coordinates (y,z). On the side borders we expect to see the largest relative error, as the paths in the small volume are more likely to escape there, than the paths in the large volume. It is also acceptable to have a larger error on the sides, as our results mostly consider the volume between the light source and detector. To see the variation we plot an average relative error $\bar{e}$, defined in Equation 13 below, and shown in Figure 12, for each (y,z) position in the slab around the x = 0 plane. At each position we compare corresponding voxels in the large and small volume, and average over the 8 voxels in the x-direction. The matrix $\mathbf{Q}$ can be reshaped from a `nbr_voxels` $\times 1$ sized matrix into a three dimensional $75 \times 75 \times 30$ sized matrix where the dimensions represent the three dimensions in the Cartesian coordinate system in Figure 11, and each element is given the same index as its corresponding voxel in the simulation volume. After this the errors can be calculated as:

$$\bar{e}(\text{y}, \text{z}) = \frac{1}{8} \sum_{i=1}^{8} e_{ijk}$$
$$e_{ijk} = \frac{|q_{ijk}^b - q_{ijk}^s|}{q_{ijk}^s} \; , \tag{13}$$

where q_{ijk} are elements at indices i, j, k in the three dimensional matrix $\mathbf{Q}$ and s and b denote results from the small and big simulation respectively. The calculated errors are plotted in Figure 12.
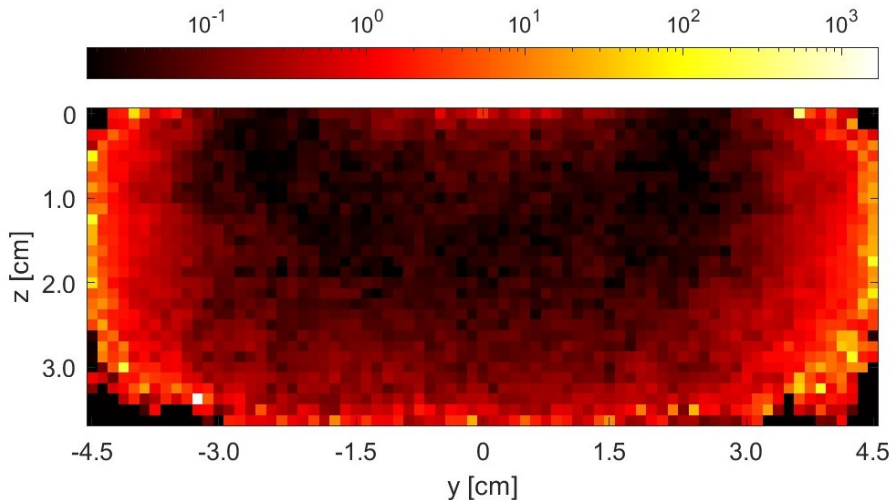

Figure 12: Relative errors between the large and small simulation volumes, calculated according to Equation 13.

As the figure shows the largest errors are on the sides and bottom of the slab, while the middle voxels have relative errors of around 10% of the signal, which is deemed acceptable. The pixels at the very bottom of the volume seem to have errors ten times the size of the signal, which must be considered when analysing the results of the simulations.

4.4 Estimating the UOT signal without simulating ultrasound-light interaction

Using matrices $\mathbf{D}$ and $\mathbf{W}$ several results can be calculated, for example the total number of detected photons from the simulation. This is just the sum of the elements in $\mathbf{W}$, corresponding to the sum of the weighted photons that were detected. We can call this number $N_{carrier}$, as it includes both tagged and not-tagged light, and define it as:

$$N_{carrier} = \sum_{i=1}^{50000} w_i \ , \tag{14}$$

where w_i is the element at index i in $\mathbf{W}$.

Furthermore, without additional simulation of ultrasound and light interaction, the matrices $\mathbf{D}$ and $\mathbf{W}$ can also be used to make an estimate of the UOT signal. In our estimate we assume that the photons have the same probability of being tagged anywhere in the simulation volume. This corresponds to an ultrasound pulse that can propagate to any position in the simulation volume without attenuating or changing its frequency. We also assume that the ultrasound amplitude is constant over the pulse volume, that is assumed to range across 5 voxels, i.e. $0.6 \times 0.6 \times 0.6$ cm^3. Finally, we assume that the probability of a photon being tagged is proportional to its pathlength within the pulse volume. Unpublished simulation results within the group have shown strong correlations between the pathlength spent within a region and the fraction of tagged photons to carriers from said region. However, similar correlations have also been found when different exponents are given to the pathlength, making the detailed relation yet unsure. For this estimation a simple proportional relationship between pathlength and probability of tagging is assumed. Thus, the pathlength propagated within each voxel is used to estimate the number of tagged photons generated.

From these assumptions, we create a matrix $\mathbf{S}$ of size `nbr_voxel`$\times 1$, containing the number of tagged photons from each voxel:

$$\mathbf{S} = \eta \, \mathbf{D}^T \mathbf{W} \ , \tag{15}$$

where the scalar η is the spatially invariable probability of tagging, which is set to 40 m^{-1} for all estimations in this chapter. A spatially invariable probability of tagging means that attenuation of the ultrasound pulse was not accounted for in the calculations. The number of tagged photons should be viewed as dependent on the number of initialised paths Z, i.e. the number of photons irradiated from the light source. The UOT signal can therefore also be expressed as the number of tagged photons per input photon, or $\frac{1}{Z}\mathbf{S}$ to enable comparisons between different simulations.

To gain information about the maximum possible signal, the number of tagged photons from each voxel can be scaled to the maximum number of input photons. This input is governed by the medical safety limit, which is about 200 mW/cm^2 for 800 nm light irradiated into tissue [50]. For our 5 mm radius light source this power corresponds to 6×10^{17} photons/second. We assume that `num_paths` is large enough for the simulation results to be statistically accurate, which would mean that the number of tagged photons from each voxel scales linearly with the number of input photons.

However, even if 6×10^{17} photons are sent into the tissue every second, the window of time during which tagging occurs may be much smaller than one second. The current imagined UOT setup includes an ultrasound pulse propagating down from an outer surface, through the tissue in a straight line, while tagging occurs as it propagates. An image would consist of several such

lines, as the ultrasound transducer activates different elements along its array (see section 2.2). If we consider the speed of sound in tissue to be about 1480 m/s, i.e. the same as in water, and if we consider the resolutions desired to be in the order of $\sim$mm, the ultrasound can be estimated to spend about $t = \frac{10^{-3} \text{ m}}{1480 \text{ m/s}} \approx 0.7$ µs ≈ 1 µs in each voxel, as it traverses through the tissue. Thus, even though the tissue is being illuminated with 6×10^{17} photons per second, only the photons irradiated during approximately one microsecond can be tagged in any given voxel. If this is too little, we may consider revisiting each voxel several times to collect multiple rounds of signals. In this case the size of the signal is limited to the number of times the ultrasound pulse can revisit each voxel per second. We assume that the minimum number of voxels required in an image is 1000 voxels, which would correspond to a $10\times10\times10$ voxel image in 3D. If 1 µs is spent on each of the 1000 voxels, the ultrasound pulse could revisit every voxel 1000 times per second.

Considering all this, from a 6×10^{17} photons per second input, only photons irradiated during one millisecond can be tagged in a given voxel. As one goal of UOT is to perform real-time imaging, we assume that the time spent on each 1000 voxel image is in the order of seconds. The maximum number of tagged photons per second from each voxel can then be calculated as:

$$\mathbf{S}_{max} = \frac{1}{Z} \times 6 \times 10^{17} \times 10^{-3} \times 10^{-2} \times \eta \times 5^3 \times \mathbf{D}^T \mathbf{W} , \tag{16}$$

where η is the probability of tagging that we have assumed, and the factor 10^{-2} represents all additional losses in the UOT setup, including cable losses, losses from coupling between light guides and detectors, etc. In the current lab setup these losses are as large as a factor of 10^{-4}, but here an optimistic estimate is assumed, corresponding to all components of the setup having been optimised. The factor 5^3 in Equation 16 accounts for the size of the ultrasound pulse being 5 times larger than our voxels in every direction. Instead of adding the pathlengths of 5^3 voxels we consider the signal in each voxel and estimate the result if $5\times5\times5$ voxels all had this signal.

4.5   Results

Figure 13 shows an example of the simulation results. The figure shows the estimated number of tagged photons per input photon from each $0.12\times0.12\times0.12$ cm^3 sized voxel, in a cross section of the simulation volume along the x = 0 plane. Figure 13a shows a simulation in the adult volume, and Figure 13b in the infant volume. Both simulations were made with the light source-detector separation $L = 2$ cm.

(a) Adult simulation volume
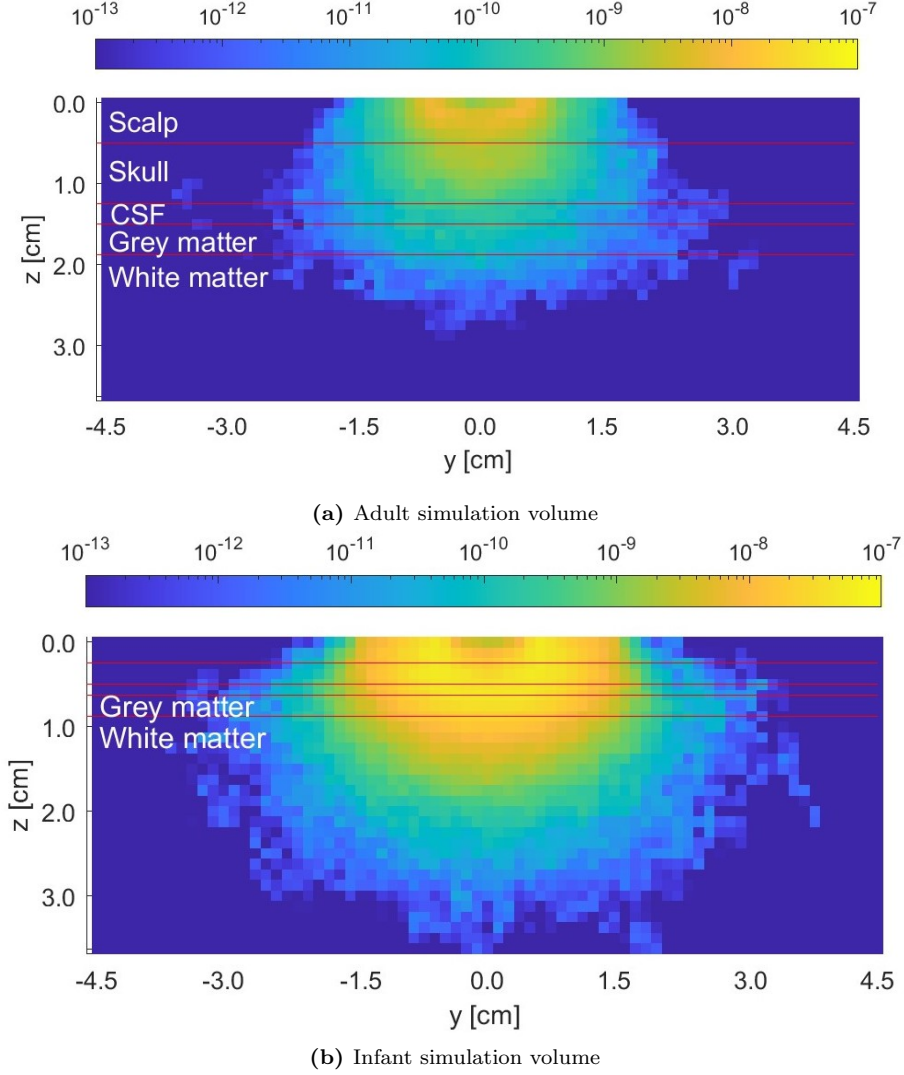

(b) Infant simulation volume

Figure 13: Estimated number of detected tagged photons per input photon from each voxel (corresponding to the contents of $\frac{1}{Z}\mathbf{S}$, defined in Equation 15) in the $L = 2$ cm simulation. The figures show a cross section in the x = 0 plane (see Figure 11). The red lines indicate borders between tissue layers.

The infant simulation appears to result in larger signals from the brain matter than the adult simulation. The figure also shows that the largest number of tagged photons originate from the volume between the source and the detector (i.e. the y-coordinates between the light source and detector). All simulations showed this, regardless of the value of L. Therefore, the y-coordinates around y = 0 were considered when evaluating penetration depth from the simulations.

When estimating the signal strength from each depth (i.e. from each z-coordinate) in the simulation volume, ten y-coordinates around y = 0 were considered, corresponding to ten lines parallel to the z-axis in Figure 13. Each line contained 30 depths, as this was the number of voxels contained in

34

the simulation volume in the z-dimension. At each depth the number of tagged photons per input photon, i.e. the contents of $\frac{1}{Z}\mathbf{S}$ (defined in Equation 15), were averaged over the ten y-coordinates.

Additionally, the signal-to-noise ratio (SNR) can be calculated at each of the 30 depths. This was done by comparing the average (over the ten y-coordinates) number of tagged photons detected from each depth to the shot noise from all detected photons. The SNR without any filtering would be very low, but frequency filters are currently used to reduce the noise from carrier light, as mentioned in section 1.1. Therefore filtering was accounted for in the SNR calculations. As previously mentioned, the filters currently used are 25 dB filters, corresponding to a $10^{-2.5}$ attenuation of the carrier light. However, more powerful filters with 40 dB attenuation capacity are available at other wavelengths [2] and development of such filters is ongoing. Therefore, optimistic SNR estimates were made with 40 dB filtering of the carrier light:

$$\text{SNR} = \frac{N_{tagged}}{\sqrt{N_{carrier} \times 10^{-4} + N_{tagged}}} \ , \tag{17}$$

where N_{tagged} is the averaged number of tagged photons detected from each depth and $N_{carrier}$ is the total number of photons detected as defined in Equation 14.

The SNR can be expressed as a measure per square root input photon $\sqrt{Z}$, by dividing both the number of tagged photons N_{tagged} and the number of carriers $N_{carriers}$ with the number of input photons Z. The maximum achievable SNR can then be calculated by scaling both N_{tagged} and $N_{carrier}$ by the maximum number of input photons per second (which previously was estimated to be $6 \times 10^{17} \times 10^{-3} \times 10^{-2}$ photons per second).
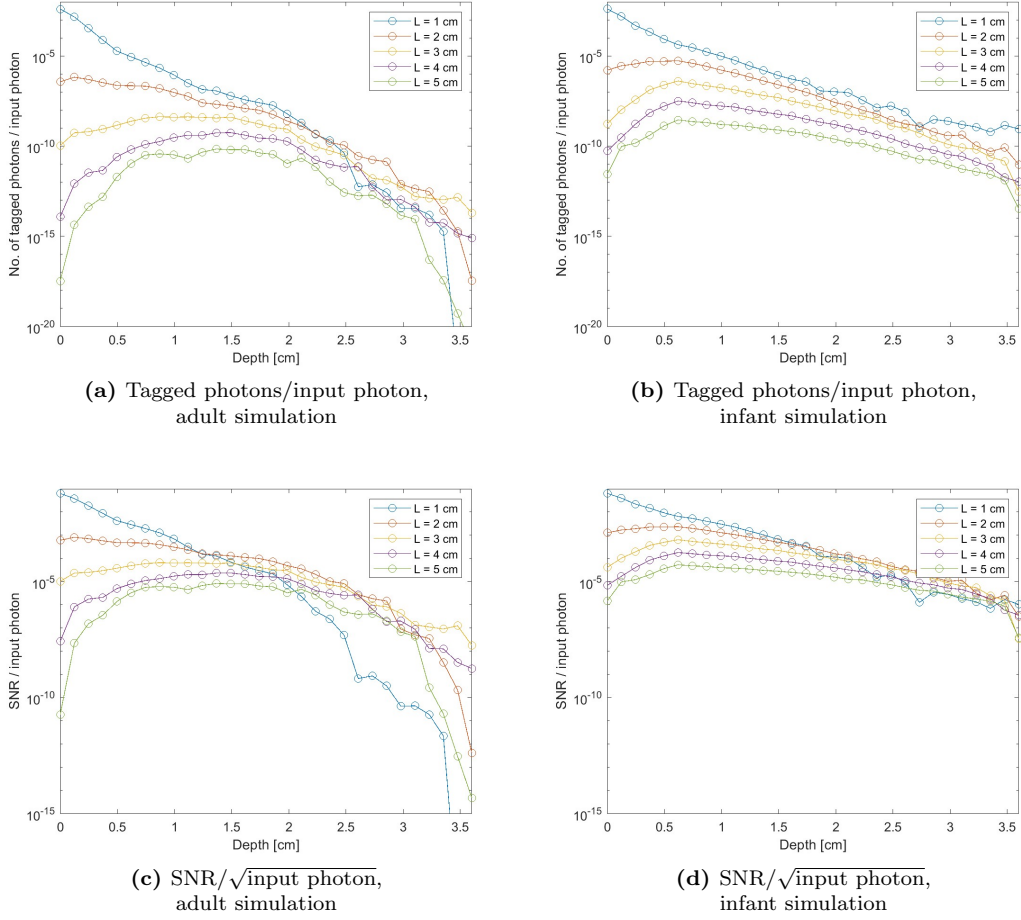
(a) Tagged photons/input photon,
adult simulation

(b) Tagged photons/input photon,
infant simulation

(c) SNR/$\sqrt{\text{input photon}}$,
adult simulation

(d) SNR/$\sqrt{\text{input photon}}$,
infant simulation

Figure 14: The estimated number of tagged photons per input photon, and the resulting SNR per square root input photon, from each ultrasound pulse sized voxel ($0.6{\times}0.6{\times}0.6$ cm^3), plotted over depth (i.e. the z-axis in the simulation volume). The results are from the x = 0 plane in the simulation volume, and the signal from each depth is averaged over 10 y-coordinates around y = 0. The number of tagged photons is estimated according to Equation 15, where the probability of tagging is assumed to be proportional to the pathlength spent inside the ultrasound pulse, with a coefficient of proportionality $\eta = 40$ m^{-1}. The SNR is calculated according to Equation 17 and then divided by $\sqrt{Z}$. Each curve shows the result from a simulation with a certain light source-detector separation L. These plots can be used to estimate the maximum achievable signal at each depth by multiplying with the assumed maximum number of input photons after considering all system losses: $6 \times 10^{17} \times 10^{-3} \times 10^{-2} = 6 \times 10^{12}$ photons per second. The maximum achievable SNR at each depth can be estimated by multiplying the plots with the square root of this number.

Figure 14 shows results from five simulations with light source-detector separations 1 cm, 2 cm, 3 cm, 4 cm, and 5 cm. The curves show the number of tagged photons detected per input photon and the SNR per square root input photon from each of the 30 depths (averaged over ten y-coordinates, as described above), in both the adult and infant simulations. From the figures it is apparent that the light simulated in the infant head generates both higher signal-to-noise ratios

and a higher number of tagged photons, than the light simulated in the adult head.

Comparing only the adult simulations, the optimal separation distance L can be found for different depths. If only signal strength, i.e. number of detected tagged photons is considered, Figure 14a shows that for depths z $\leq$ 2 cm the optimal separation is $L = 1$ cm. For depths between 2.3 and 3.3 cm the optimal separation appears to be $L = 2$ cm, and for depths z $\geq$ 3.3 cm the optimal separation is $L = 3$ cm. The infant simulations in Figure 14b show more consistency, with the separation $L = 1$ cm being optimal at every depth. Thus, the sudden decrease in signal from depths z $\geq$ 2.3 cm for the $L = 1$ cm adult simulation appears to deviate from the other curves in Figure 14a-b. Possible explanations for this will be discussed in section 4.6

If instead the SNR is considered, Figures 14c and 14d show that $L = 1$ cm is only the optimal separation for depths z $\leq$ 0.5 cm, and at large depths it becomes the worst performing separation distance. Between depths of about 0.5 and 1.5 cm the optimal separation distance appears to be $L = 2$ cm for both infant and adult simulations, and at larger depths it is unclear which of the separations performs best.

4.5.1 Estimating penetration depth

We would like to estimate the penetration depth, i.e. the largest depth z at which imaging is possible, for each of the separations L. To do this we consider SNR $= 100$ to be the minimum required for imaging. This number can be changed, but the SNR should be high enough for optical contrasts to be distinguishable. We also assume that our setup is shot noise limited, which would mean that Equation 17 includes all the detected noise, although this is not the case in the real UOT setup. A minimum of 10 000 detected tagged photons would be required from each voxel for the SNR to not dip below 100 due to shot noise from the tagged photons alone.

As previously mentioned, the maximum achievable signal strength and SNR at each depth can be estimated from the results shown in Figure 14 by scaling the curves with the assumed maximum number of input photons per second $6 \times 10^{17} \times 10^{-3} \times 10^{-2} = 6 \times 10^{12}$. From our requirements, the maximum achievable signal strength has a cutoff at 10 000, while the maximum achievable SNR has a cutoff at 100. Considering this, Figure 15 shows the estimated maximum achievable penetration depth plotted over the light source-detector separations L that were simulated.
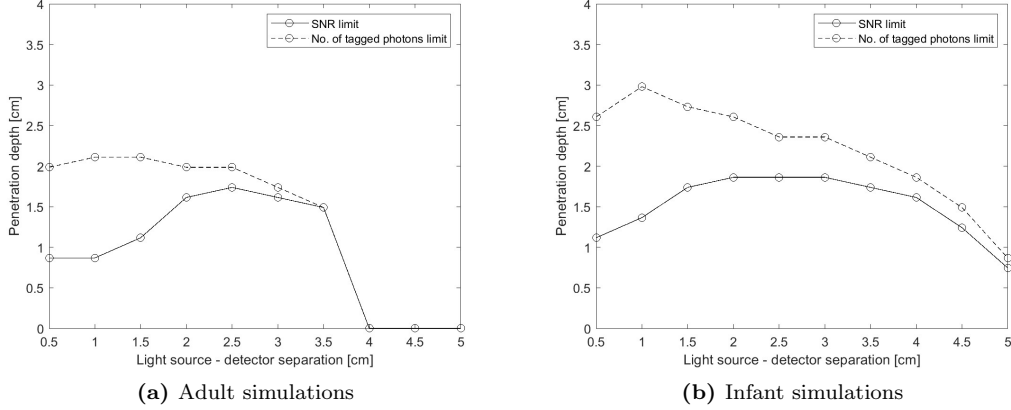
(a) Adult simulations

(b) Infant simulations

Figure 15: Estimated penetration depths plotted over the separation distance L between light source and detector. The number of tagged photons and SNRs from each depth was calculated in the same way as in Figure 14, but were scaled by the assumed maximum number of input photons per second, $6 \times 10^{17} \times 10^{-3} \times 10^{-2} = 6 \times 10^{12}$.

The estimated curves show that the 40 dB frequency filters would achieve imaging to about 1.5 cm and 2 cm depths for adult and infant heads, respectively. If perfect filtering of the tagged photons was achievable however, the curves show that the maximum imaging depth would be about 2 cm and 3 cm for adult and infant heads, respectively.

4.5.2 Absorbance of each tissue layer

From the simulated paths we can also investigate how far the photons travel in each tissue layer. This can be achieved by comparing the average pathlength l that the detected photons propagated in each layer:

$$l_m = \frac{1}{50000} \sum_{k \in D_m} \sum_{j=1}^{75} \sum_{i=1}^{75} q_{ijk} \;, \tag{18}$$

where q_{ijk} is the element at index i, j, k in the reshaped matrix $\mathbf{Q}$ (see section 4.3) and D_m is the set of indices contained within domain/tissue type m. Figure 16 shows a barplot of the average optical pathlengths l that the photons spent in each tissue layer m for adult and infant simulations with two different separations, $L = 2$ cm and $L = 5$ cm. Note that these numbers do not account for absorption of the photons.
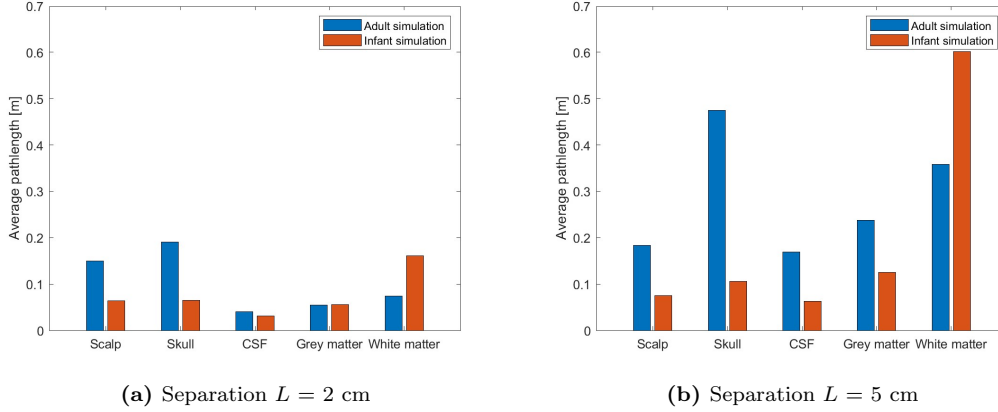
(a) Separation $L = 2$ cm   **(b)** Separation $L = 5$ cm

Figure 16: Average pathlength spent in each tissue layer, calculated according to Equation 18. The figures include simulations from the adult and infant head, with light source-detector separations (a) 2 cm and (b) 5 cm.

Several things can be noted about the results plotted in these diagrams. Firstly, the smaller separation L appears to result in generally shorter average pathlengths. This may be the reason why the signal is stronger in the simulations with smaller L, as shorter pathlengths correspond to less absorption of the photons (see Equation 10). The distribution of pathlengths between different tissue layers, however, seems to be similar for the two separations. Lastly, the photons in the infant simulation clearly spend less time in the scalp and skull layer, and more time in the layer of white matter. This makes sense, as the infant simulation volume has a thicker layer of white matter and thinner layer of scalp and skull. It may also explain the larger signal strength in the infant simulations, as the scalp and skull may absorb less of the signal before it reaches the detector.

Some statements in the discussion above can be tested by calculating how much light each layer absorbs. Even though we already know the absorption coefficient μ_a of each tissue layer, the pathlengths spent inside them also affect the absorption, according to Equation 10. One way of comparing the tissue layers is to calculate the absorbance A of each layer:

$$A = l \times \mu_a \, , \tag{19}$$

which combines the absorption coefficient μ_a of a medium with the pathlength l spent inside it. The absorbance of each tissue layer was thus estimated by multiplying their respective absorption coefficients with the average optical pathlengths shown in Figure 16.

Figure 17 shows the estimated absorbance of each tissue layer for adult and infant simulations with the separations $L = 2$ cm and $L = 5$ cm.
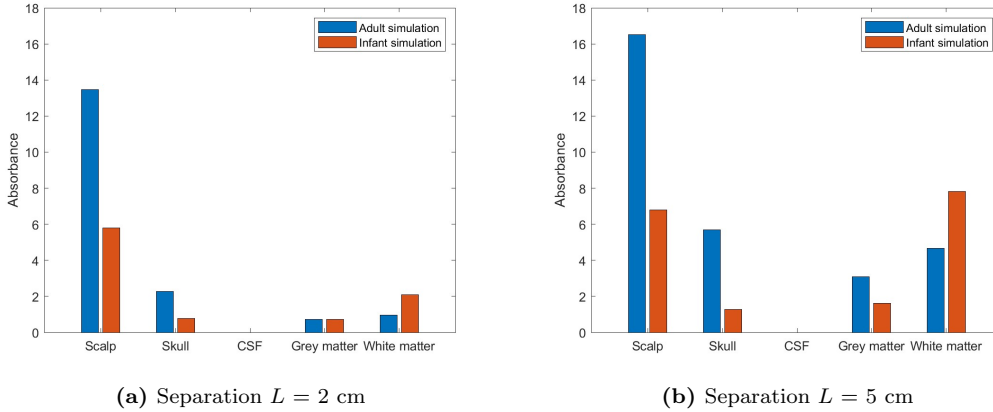
39

(a) Separation $L = 2$ cm   **(b)** Separation $L = 5$ cm

Figure 17: Absorbance of each tissue layer, calculated by inserting the pathlengths shown in Figure 16 into Equation 19. The figures include simulations from the adult and infant head, with 2 cm light source-detector separation, as well as simulations from the adult and infant head with 5 cm light source-detector separation.

As stated in the discussion above, the diagrams show that absorbance of each layer is lower in the $L = 2$ cm simulation than in the $L = 5$ cm simulation. In both adult simulations the scalp layer has the largest absorbance by far, which seems reasonable as its absorption coefficient is larger than the other layers' (see Table 7). This may indicate that the optimal positions on the head for UOT imaging are positions where the skin is thin. The diagrams also confirm that the absorbance of each layer is lower in the infant simulations, apart from that of the white matter layer.

4.6 Discussion

The main uncertainty regarding the results from the simulations of light propagation in the head is still the optical properties of the tissues. Although a more thorough literature search was conducted for the optical properties of brain matter, all inconsistencies can not be reconciled simply by reading. As most of the focus was put on finding the coefficients of brain matter, the studies concerning scalp and skull were not as thoroughly compared and evaluated. Particularly uncertain is the absorption coefficient of scalp. This coefficient depends on the melanin content in the epidermis, which varies greatly between individuals. As Figure 17 shows, the skin is responsible for much of the loss of signal, so the absorption coefficient of the skin may have a large effect on the simulation results. As before, further investigation of the optical parameters of the tissues is needed.

The outcome of the simulation also depends on the thicknesses of the different tissue layers included in the simulation volume. As mentioned in section 4.2, the thicknesses of the layers in the adult volume were chosen to represent a piece of forehead. However, different positions on the human head with different thicknesses of the scalp and skull may give other results. From the results imaged in Figure 17, we could theorize that the optimal position to illuminate is a place where the skin is thin, although this might change if the selected absorption coefficient of skin was incorrect.

Apart from these error sources of the simulation, there are limitations to the estimated UOT signal strengths and SNRs. As previously mentioned, the estimates are based on the assumption that the ultrasound pulse would have the same amplitude and pressure distribution anywhere in

the simulation volume. By considering the results from section 2.4, we can speculate that this is not accurate. The probability of tagging, per pathlength spent inside the ultrasound pulse, $\eta = 40$ m^{-1}, may also be inaccurate. These assumptions will be evaluated in chapter 5 when a simulation of ultrasound-light interaction is conducted.

With these reservations in mind, the estimates from the simulations in this chapter can still be analysed. In section 4.5 the optimal light source-detector separations L were stated for different depths in the adult or infant head. If only signal strength was considered, the optimal separation appeared to be $L = 1$ cm for the infant simulations, at any depth, and $L = 1$ cm for the adult simulations up to about 2.3 cm depth. The sudden decrease in signal from depths larger than 2.3 cm for the adult $L = 1$ cm simulation appears to deviate from the other curves in Figure 14a-b. The rest of the curves seem to show that the smaller the separations, the larger the signals. However, recall that the number of input photons Z is not the same in the different simulations. The simulations with smaller separations L initiated about 10^6 paths, whereas the simulations with the largest separations L initiated up to 10^8 paths. It is possible that the number of initiated paths in the $L = 1$ cm simulation is too small to show the number of photons propagating to larger depths with statistical accuracy. This may be true particularly in the adult simulation volume where fewer photons propagate to the depths of the volume and return. In other words, it is possible that the $L = 1$ cm plot in Figure 14a is misleading.

The results from the infant simulations seem to show some trade-off between SNR and signal strength. If perfect filters were available and the only limit was shot noise from the tagged photons, a shorter distance such as $L = 1$ cm could be chosen for a better result. However with a 40 dB filter, the curves show that a larger distance, such as $L = 2$ cm or 3 cm would perform better at larger depths.

Figures 15a and b use the results in Figure 14, scaled by an assumed maximum achievable number of input photons, to estimate penetration depths into the brain. For the infant head the estimated depth is somewhat optimistic. If filters can be made better, making the main limitation shot noise from the tagged photons, Figure 15b shows an estimated penetration depth of 3 cm, which would cover a large part of the radius of an infant head (which is about 5 cm).

Even with the optimal light source-detector separations though, the results in Figure 15a indicate that brain imaging in the adult head would be challenging. With perfect frequency filters, the number of detected tagged photons are estimated to limit the penetration depth to 2 cm, which corresponds to the interface between the grey matter and white matter layers in the adult simulation volume. This would mean that most of the brain volume is unreachable. However, several aspects of the simulated UOT setup can be improved.

For example, the maximum number of input photons per second can be increased by changing the area of the light source. The maximum interaction time between photons and ultrasound in each voxel (here estimated to be 1 ms) is dependent on the resolution and size of the images, which can be freely selected (see calculations in section 4.4). The detector area could also be increased, and the assumed tagging probability per pathlength $\eta = 40$ m^{-1} depends on ultrasound parameters that are alterable. Another possible adjustment is the time scale of the imaging. If the irradiation and detection time is increased to be longer than one second, a greater number of tagged photons could be collected, although this would compromise the ability to perform real-time imaging. Due to these possible improvements, and the remaining uncertainty regarding several of the optical parameters used, we conclude that further investigation is needed.

5 Simulation with ultrasound

This chapter describes the second part of the Monte Carlo simulations, which is the simulation of ultrasound-light interaction. We begin by shortly describing the principles behind the simulation (for a proper explanation see Ref. [2]) in section 5.1, after which the results of the simulation are presented in section 5.2. Due to time constraints the ultrasound-light interaction could only be modelled in a limited sub-volume of the entire simulation volume, and for only one single light source-detector separation L. Therefore the focus will mainly be to compare the estimated UOT signal from section 4.4 to the UOT signal that is simulated here.

5.1 Modelling ultrasound-light interaction

The ultrasound is in this simulation defined as

$$P(\mathbf{r}, t) = L(x, y) \times G(vt - z + z_0) \times p(t, z) , \qquad (20)$$

where function $L(x, y)$ is the Lorentzian distribution described in Equation 6, G is the supergaussian defined in Equation 5, and p is the superposition of plane waves defined in Equation 4. All parameters included in Equation 20 are based on the measurements in chapter 2 and defined at 15 values of z in Table 1. The parameters in Table 1 were also used to interpolate the pulse characteristics at values of z between the 15 measurement points. Unfortunately, due to a mistake not discovered until all simulations were finished, the length of the pulse in the z-direction was made to be half of the value estimated from the experimental measurements in chapter 2. While the estimation made in section 2.5 was $\sigma_z = v\sigma_t = 1480 \times 0.74 \times 10^{-6} \approx 1$ mm, the value used in our simulations was $\sigma_z \approx 0.5$ mm (the wavelength of the ultrasound in water is about $\lambda \approx 0.25$ mm). However, as the duration of the pulses can be adjusted by the transducer, this was not deemed to be unrealistic or invalidating of the simulation results.

As previously mentioned, in section 1.1, the ultrasound-light interaction causing the frequency shifting is explained partly by the periodic displacement of scattering particles in the medium, and partly by the periodic perturbation of the refractive index in the medium. The former of these phenomena can be modelled by considering the set of points at which a simulated photon path m is scattered and changes direction: $\mathbf{R}_m = \mathbf{r}_{m,1}, ..., \mathbf{r}_{m,J_m}$, and by expressing their displacement as a function of the ultrasound pressure amplitude $\mathbf{A}$:

$$\mathbf{r}_{m,j}(t) = \mathbf{r}_{m,j} + \mathbf{A}(\mathbf{r}_{m,j}, t) , \qquad (21)$$

where $\mathbf{r}_{m,j}$ is the spatial coordinates of scattering point j in photon path m, and t is the time. The second phenomenon, i.e. the change of the refractive index $\mathbf{n}$ in the medium, can be quantitatively described as

$$\mathbf{n}(\mathbf{r}, t) = \mathbf{n}_0 \left[1 + \frac{\partial \mathbf{n}}{\partial P} P(\mathbf{r}, t) \right] , \qquad (22)$$

where $\mathbf{n}_0$ is the refractive index at pressure equilibrium, $\frac{\partial \mathbf{n}}{\partial P}$ is the piezo-optic coefficient, which is assumed to be $\frac{\partial \mathbf{n}}{\partial P} = 1.466 \times 10^{-10}$ Pa^{-1} as it is in water [51], and $P(\mathbf{r}, t)$ is the ultrasound pressure (with amplitude $\mathbf{A}$).

Combining these two interactions, the resulting time varying phase $\phi_m(t)$ for a path m can be expressed as

$$\phi_m(t) = k_C \sum_{j=1}^{J_m} \int_0^{L_{m,j}(t)} \mathbf{n}[x_{m,j}(t, l), t] \, dl , \qquad (23)$$

where k_C is the optical wave number of the unshifted light in vacuum, $L_{m,j}(t)$ is the free-path length, i.e. the distance between scattering points of indices $[m, j]$ and $[m, j - 1]$, $\mathbf{x}$ is the free pathlength coordinate, and $l \in [0, L_{m,j}(t)]$. From the phases ϕ_m a power spectral density spectrum can be calculated, and the number of tagged photons and carrier photons are estimated by the power in a given frequency range by integrating over this spectrum. A more detailed description of the algorithm than this will not be given in this thesis, but can be found in Ref. [2].

The simulation is defined by a set of positions for the ultrasound pulse. At each position the interactions between the pressure P and the photon paths within an interaction range of the position are calculated. The interaction range was set to be within a 5 mm radius of the ultrasound position, which was expected to cover most of the pressure distribution of the pulse, considering the values for σ_x and σ_y between z = 0.5 cm and z = 3.5 cm (see Table 1). As the simulation volume is only 3.6 cm deep, these are the relevant parts of the ultrasound pulse.

### 5.1.1 Configuration of the simulations

Due to time constraints only a limited number of ultrasound positions could be simulated. They were chosen to resemble the sub-volume included in the estimation of penetration depth, conducted in section 4.5. Recall that ten lines along the z-axis, around y = 0, in the x = 0 plane were selected.

For the adult simulation volume, the ultrasound was simulated in 5×9 positions from y = -5 mm to y = 5 mm, and from z = 1.3 cm to z = 3.6 cm. Only positions from z = 1.3 cm were considered, as the brain is the main region of interest, and 1.3 cm this is the depth of the cerebrospinal fluid layer in the simulation volume. For the infant simulation volume the ultrasound was simulated from z = 0.6 cm to z = 3.6 cm, as 0.6 cm is the depth of the infant cerebrospinal fluid layer. This corresponds to 5×11 ultrasound positions.

The photon paths that were included in this part of the simulation came from the light propagation simulation with separation $L = 5$ cm. The results therefore represent the UOT signal from a setup where the distance between light source and detector is 5 cm.

5.2 Results

Figures 18a and 19a show the estimated UOT signal from the light propagation simulations alone, in the adult and infant volumes respectively, above Figures 18b and 19b, which show the simulated tagged photons in the first frequency sideband from the ultrasound-light interaction simulations. Note that Figures 18a and 19a correspond to what is shown in Figure 13, but for the separation $L = 5$ cm. The resolution differs between the images as the number of ultrasound positions does not correspond to the number of $0.12 \times 0.12 \times 0.12$ cm^3 voxels contained within the same volume.
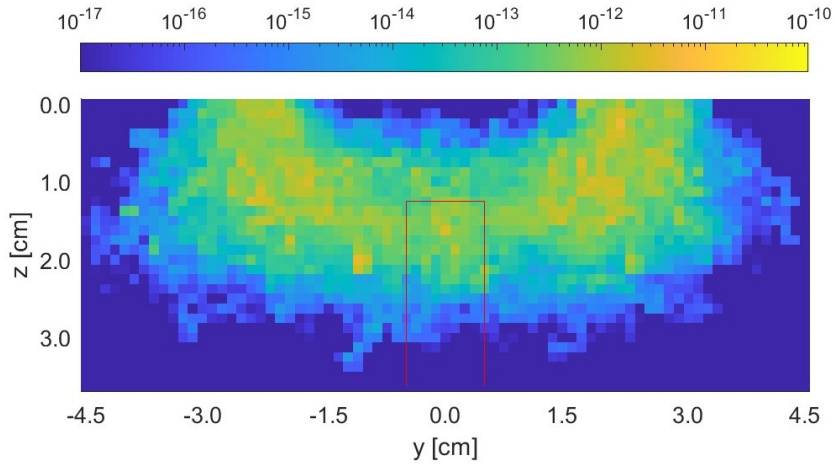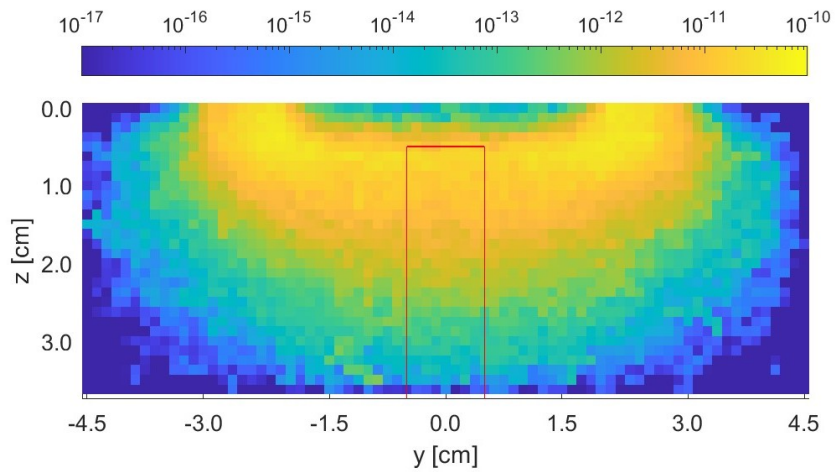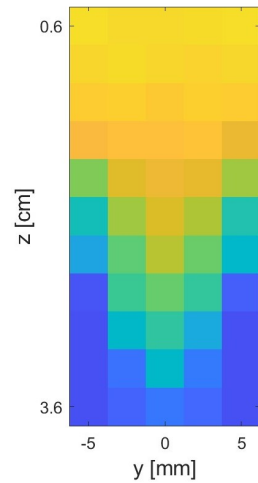
(a) Estimated signal from chapter 4.
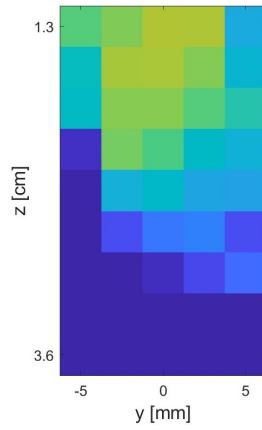
(b) Simulated signal.

Figure 18: Spatial distribution of the number of detected tagged photons per input photon in the **adult** simulation volume, with light source-detector separation $L = 5$ cm. Comparison between the estimate from the simulated photon paths alone (a), and the result from simulations of ultrasound-light interaction (b). The red lines in (a) show the location of the sub-volume shown in (b). However, the dimensions do not match exactly, due to rounding errors as the pixel sizes in the two images are not the same. The two figures are plotted with the same color scale.

(a) Estimated signal from chapter 4.

(b) Simulated signal.

Figure 19: Spatial distribution of the number of detected tagged photons per input photon in the **infant** simulation volume, with light source-detector separation $L = 5$ cm. Comparison between the estimate from the simulated photon paths alone (a), and the result from simulations of ultrasound-light interaction (b). The red lines in (a) show the location of the sub-volume shown in (b). However, the dimensions do not match exactly, due to rounding errors as the pixel sizes in the two images are not the same. The two figures are plotted with the same color scale.

At first glance, the figures seem to show quite good agreement in signal strength between the estimates and the simulated results in both the infant and adult simulation volume, i.e. the order of magnitude of the detected number of tagged photons per input photon seems to be about the same. However, the sizes of the pixels in Figures 18a and 19a (0.12×0.12 cm^2) are smaller than the pixels in Figures 18b and 19b ($\sim 0.25 \times 0.3$ cm^2). Therefore, the same colors in Figures 18a and 19a, correspond to a larger number of tagged photons than in 18b and 19b, by a factor of $\sim \frac{0.25 \times 0.3}{0.12^2} \approx 5$. This has not been accounted for in the figures.

Comparing Figures 18a and b, we can also see that the color gradient in the z-direction appears to be quite similar in the two results. As is the case in Figure 19, especially if the y coordinates $|y| \leq 2.5$ mm are considered.

However, there are some discrepancies between the estimations based on light propagation simulations alone, and the results from the simulation of ultrasound-light interaction. For example, although Figure 19a shows that the pathlengths spent in the voxels around $|y| > 2.5$ mm are in the same order of magnitude as the ones in the voxels around y = 0, Figure 19b shows a steeper color gradient at $y = \pm 5$ mm. This may be explained by the fact that the ultrasound pulse has an interaction range of 5 mm (as mentioned in section 5.1). By viewing Figure 19a, we can see the pathlengths spent in voxels within 5 mm of the ultrasound positions $y = \pm 5$ mm. These voxels have somewhat steeper color gradients, which might explain the appearance of Figure 19b.

5.3   Discussion

The most interesting aspect of the results is whether or not the assumption that the probability of tagging is proportional to the pathlength spent in each voxel is valid. The similar color gradients along the z-axis seem to indicate that it is, although there are some discrepancies. It would also indicate that the assumption of a spatially invariable probability of tagging per pathlength, η, is approximately true within the depth investigated here. This result might be explained by the measurement results from chapter 2. The ultrasound-light interaction has been simulated between $z \approx 0.5$ cm or $z \approx 1.0$ cm to $z \approx 3.5$ cm, and from Figure 8 we can see that the skull pulse, which was used to model the ultrasound pulse, does not attenuate much within these distances from the transducer. In fact, according to the calculated energies, the skull pulse keeps over 80% of its energy from z = 0.5 cm to z = 3.5 cm. This might be why the assumption of a spatially invariable probability of tagging appears to be correct.

Thus, the simulation results from this chapter support the estimates of the UOT signal in chapter 4, apart from a difference in η by a factor of 5. However, as this is less than one order of magnitude, no recalculations of the estimates from chapter 4 will be made.

As the analytic expression of the ultrasound pulse in these simulations was based off the measurements described in chapter 2, the accuracy of these measurements will also dictate the accuracy of the simulation results. Although the measurements showed the propagation of an ultrasound pulse after passing through skull bone, they did not measure attenuation through any other tissue contained in the human head. In other words, our simulations do not account for attenuation in brain tissue, but instead assumes that it is the same as in water. Furthermore, as the skull bone used in the measurements originated from an infant cranium, the results from the adult simulation volume probably overestimate the generated UOT signal. This is because an adult cranium would be thicker, causing the transmitted ultrasound pulse to have a smaller amplitude.

On the other hand, as stated in section 2.3, the powering voltage used (18 V) was well below the maximum input voltage for the transducer (24 V), even though both voltages generated pressures below the medical safety limit (see Figure 4). The voltage could therefore be increased, which could result in higher pressure amplitudes and greater probabilities of tagging.

6 Conclusions

The purpose of this thesis was to asses the conditions for ultrasound optical tomography inside the human brain partly by experimentally characterizing an ultrasound pulse after propagating through a 1.5 mm thick piece of skull bone originating from an infant cranium, and partly by simulating light propagation and ultrasound-light interaction in a representation of a part of the human head.

The experimental measurements showed a strong attenuation of the ultrasound pulse from its propagation in the skull, with energy losses estimated to be about 80-90%. However, the pulse shape was not severely distorted. These results are mostly relevant to imaging in the infant head, as no adult skull bone was included in the measurements.

As for the propagation and tagging of photons inside the head, two sets of simulations were conducted, namely one inside a representation of an adult head and one an infant head. The simulations tested ten different separation distances between light source and detector from 0.5 cm to 5 cm and found that the smaller distances (between 1-2.5 cm) resulted in larger numbers of detected tagged photons and larger signal-to-noise ratios. Rough estimates of penetration depths in an assumed shot noise limited ultrasound optical tomography setup, with perfect frequency filters, were calculated to be ≤ 2 cm for the adult head (achieved with 1-1.5 cm light source-detector separation) and ≤ 3 cm for the infant head (achieved with 1 cm light source-detector separation). For the adult head this corresponds to reaching the layer of grey matter and some superficial white matter in the brain, while the penetration depth for the infant head reaches parts of the white matter. The difference in penetration depth between the adult and infant head is most likely due to the infant having thinner layers of scalp and skull. The photons travel longer pathlengths in the scalp- and skull-layers of the adult simulation, resulting in larger absorbance and a weaker signal.

Thus, the results from this thesis indicate that the conditions for imaging in the adult head seem challenging, while the conditions in the infant brain seem somewhat better. However, several aspects of the setup that were assumed here can be adjusted for more optimistic estimates, including light source and detector area, head location (as thicknesses of scalp and skull vary across the head), as well as the time during which the signal is collected, although this would mean that the imaging might not be performed in real-time anymore.

Further investigation of the optical properties of tissues in the head are necessary for more reliable conclusions. Measurements of ultrasound propagation in brain matter phantoms would complement the measurements in this thesis, as well as measurements of ultrasound propagation through an adult skull bone. Lastly, further simulations of heads including inclusions with deviating absorption properties could investigate the achievable contrast in brain imaging.

7 References

[1] Victor F. Humphrey. "Ultrasound and matter—Physical interactions". In: *Progress in Biophysics and Molecular Biology*. Effects of ultrasound and infrasound relevant to human health 93.1 (Jan. 1, 2007), pp. 195–211.

[2] David Hill. "Development of Models, Methods, and Materiel for Deep Tissue Imaging using Light, Ultrasound, and Spectral-Hole Burning". PhD thesis. Lund University, 2022.

[3] Alexander Bengtsson. "Material and technique development for ultrasound optical tomography using spectral hole burning filters". PhD thesis. Lund University, 2022.

[4] Francis A. Duck. "Nonlinear acoustics in diagnostic ultrasound". In: *Ultrasound Med Biol* 28.1 (Jan. 2002), pp. 1–18.

[5] Caroline Boudoux. *Fundamentals of Biomedical Optics*. Blurb, 2024.

[6] Sabrina Brigadoi and Robert J. Cooper. "How short is short? Optimum source–detector distance for short-separation channels in functional near-infrared spectroscopy". In: *NPh* 2.2 (May 2015), p. 025005.

[7] Guilherme Augusto Zimeo Morais, Joana Bisol Balardin, and João Ricardo Sato. "fNIRS Optodes' Location Decider (fOLD): a toolbox for probe arrangement guided by brain regions-of-interest". In: *Sci Rep* 8.1 (Feb. 20, 2018), p. 3341.

[8] Tzu-Chia Kao and Kung-Bin Sung. "Quantifying tissue optical properties of human heads in vivo using continuous-wave near-infrared spectroscopy and subject-specific three-dimensional Monte Carlo models". In: *JBO* 27.8 (June 2022), p. 083021.

[9] Joakim Jönsson and Edouard Berrocal. "Multi-Scattering software: part I: online accelerated Monte Carlo simulation of light transport through scattering media". In: *Opt. Express, OE* 28.25 (Dec. 7, 2020), pp. 37612–37638.

[10] C. Mignon et al. "Shedding light on the variability of optical skin properties: finding a path towards more accurate prediction of light propagation in human cutaneous compartments". In: *Biomed. Opt. Express, BOE* 9.2 (Feb. 1, 2018), pp. 852–872.

[11] C. Rebecca Simpson et al. "Near-infrared optical properties of ex vivo human skin and subcutaneous tissues measured using the Monte Carlo inversion technique". In: *Phys. Med. Biol.* 43.9 (Sept. 1998), p. 2465.

[12] San Wan, R. Rox Anderson, and John A. Parrish. "Analytical Modeling for the Optical Properties of the Skin with in Vitro and in Vivo Applications". In: *Photochemistry and Photobiology* 34.4 (1981), pp. 493–499.

[13] Anne Hayman et al. "Clinical and Imaging Anatomy of the Scalp". In: *Journal of computer assisted tomography* 27 (May 1, 2003), pp. 454–9.

[14] Frédéric Bevilacqua et al. "In vivo local determination of tissue optical properties: applications to human brain". In: *Appl. Opt., AO* 38.22 (Aug. 1, 1999), pp. 4939–4950.

[15] Jee Hyun Choi et al. "Noninvasive determination of the optical properties of adult brain: near-infrared spectroscopy approach". In: *JBO* 9.1 (Jan. 2004), pp. 221–229.

[16] Alexey N. Bashkatov et al. "Optical properties of human cranial bone in the spectral range from 800 to 2000 nm". In: *Saratov Fall Meeting 2005: Optical Technologies in Biophysics and Medicine VII*. Saratov Fall Meeting 2005: Optical Technologies in Biophysics and Medicine VII. Vol. 6163. SPIE, July 21, 2006, pp. 306–316.

[17] Stefan Tauber et al. "Lightdosimetric quantitative analysis of the human petrous bone: Experimental study for laser irradiation of the cochlea". In: *Lasers in Surgery and Medicine* 28.1 (2001), pp. 18–26.

[18] Eiji Okada and David T. Delpy. "Near-infrared light propagation in an adult head model. I. Modeling of low-level scattering in the cerebrospinal fluid layer". In: *Appl. Opt., AO* 42.16 (June 1, 2003), pp. 2906–2914.

[19] Yuich Fukui, Yusaku Ajichi, and Eiji Okada. "Monte Carlo prediction of near-infrared light propagation in realistic adult and neonatal head models". In: *Appl. Opt., AO* 42.16 (June 1, 2003), pp. 2881–2887.

[20] Shuaibin Chang et al. "Scalable mapping of myelin and neuron density in the human brain with micrometer resolution". In: *Sci Rep* 12.1 (Jan. 10, 2022), p. 363.

[21] Pieter van der Zee, Matthias Essenpreis, and David T. Delpy. "Optical properties of brain tissue". In: *Photon Migration and Imaging in Random Media and Tissues*. Photon Migration and Imaging in Random Media and Tissues. Vol. 1888. SPIE, Sept. 14, 1993, pp. 454–465.

[22] A. N. Yaroslavsky et al. "Optical properties of selected native and coagulated human brain tissues in vitro in the visible and near infrared spectral range". In: *Phys. Med. Biol.* 47.12 (June 2002), p. 2059.

[23] S. C. Gebhart, W. C. Lin, and A. Mahadevan-Jansen. "In vitro determination of normal and neoplastic human brain tissue optical properties using inverse adding-doubling". In: *Phys. Med. Biol.* 51.8 (Mar. 2006), p. 2011.

[24] Jonathan Shapey et al. "Ex vivo assessment of the optical characteristics of human brain and tumour tissue". In: *Label-free Biomedical Imaging and Sensing (LBIS) 2020*. Label-free Biomedical Imaging and Sensing (LBIS) 2020. Vol. 11251. SPIE, Feb. 20, 2020, pp. 53–58.

[25] Norihiro Honda et al. "Determination of optical properties of human brain tumor tissues from 350 to 1000 nm to investigate the cause of false negatives in fluorescence-guided resection with 5-aminolevulinic acid". In: *J Biomed Opt* 23.7 (July 2018), pp. 1–10.

[26] Kerui Li et al. "In situ detection of human glioma based on tissue optical properties using diffuse reflectance spectroscopy". In: *Journal of Biophotonics* 16.11 (2023), e202300195.

[27] Jun Zhao et al. "In vivo determination of the optical properties of infant brain using frequency-domain near-infrared spectroscopy". In: *JBO* 10.2 (Mar. 2005), p. 024028.

[28] Sonoko Ijichi et al. "Developmental Changes of Optical Properties in Neonates Determined by Near-Infrared Time-Resolved Spectroscopy". In: *Pediatr Res* 58.3 (Sept. 2005), pp. 568–573.

[29] Sandra Jasminder Arri et al. "Precision of cerebral oxygenation and hemoglobin concentration measurements in neonates measured by near-infrared spectroscopy". In: *J Biomed Opt* 16.4 (Apr. 2011), p. 047005.

[30] Lorenzo Spinelli et al. "In vivo measure of neonate brain optical properties and hemodynamic parameters by time-domain near-infrared spectroscopy". In: *Neurophotonics* 4.4 (Oct. 2017), p. 041414.

[31] A. Roggan et al. "The effect of preparation technique on the optical parameters of biological tissue". In: *Appl Phys B* 69.5 (Dec. 1, 1999), pp. 445–453.

[32] Carmen Kut et al. "Detection of Human Brain Cancer Infiltration ex vivo and in vivo Using Quantitative Optical Coherence Tomography". In: *Sci Transl Med* 7.292 (June 17, 2015), 292ra100.

[33]   Miguel Alaminos et al. "EMP3, a Myelin-Related Gene Located in the Critical 19q13.3 Region, Is Epigenetically Silenced and Exhibits Features of a Candidate Tumor Suppressor in Glioma and Neuroblastoma". In: *Cancer Research* 65.7 (Apr. 1, 2005), pp. 2565–2571.

[34]   Sean C. L. Deoni et al. "Mapping Infant Brain Myelination with Magnetic Resonance Imaging". In: *J. Neurosci.* 31.2 (Jan. 12, 2011), pp. 784–791.

[35]   Héloïse Auger et al. "Quantification of extra-cerebral and cerebral hemoglobin concentrations during physical exercise using time-domain near infrared spectroscopy". In: *Biomed Opt Express* 7.10 (Sept. 1, 2016), pp. 3826–3842.

[36]   Rachel L. Smith et al. "Increased brain microvascular hemoglobin concentrations in children with cerebral malaria". In: *Science Translational Medicine* 15.713 (Sept. 13, 2023), eadh4293.

[37]   Damilola D. Adingupu et al. "Brain hypoxia, neurocognitive impairment, and quality of life in people post-COVID-19". In: *J Neurol* 270.7 (2023), pp. 3303–3314.

[38]   W.B. Gratzer.

[39]   G.M. Hale and M.R. Querry. "Optical constants of water in the 200 nm to 200 μm wavelength region". In: *Appl. Opt.* 12 (1973), pp. 555–563.

[40]   Jianing Zhang. "On sampling of scattering phase functions". In: *Astronomy and Computing* 29 (2019).

[41]   D. A. Boas et al. "Three dimensional Monte Carlo code for photon migration through complex heterogeneous media including the adult human head". In: *Opt. Express, OE* 10.3 (Feb. 11, 2002), pp. 159–170.

[42]   Ting Li, Hui Gong, and Qingming Luo. "Visualization of light propagation in visible Chinese human head for functional near-infrared spectroscopy". In: *JBO* 16.4 (Apr. 2011), p. 045001.

[43]   Gary E. Strangman, Zhi Li, and Quan Zhang. "Depth Sensitivity and Source-Detector Separations for Near Infrared Spectroscopy Based on the Colin27 Brain Template". In: *PLOS ONE* 8.8 (Aug. 1, 2013), e66319.

[44]   Ashley C. Whiteman et al. "Investigation of the sensitivity of functional near-infrared spectroscopy brain imaging to anatomical variations in 5- to 11-year-old children". In: *NPh* 5.1 (Sept. 2017), p. 011009.

[45]   F. Babiloni et al. "A high resolution EEG method based on the correction of the surface Laplacian estimate for the subject's variable scalp thickness". In: *Electroencephalography and Clinical Neurophysiology* 103.4 (Oct. 1, 1997), pp. 486–492.

[46]   Haiyan Li et al. "Investigation of the critical geometric characteristics of living human skulls utilising medical image analysis techniques". In: *IJVS* 2.4 (2007), p. 345.

[47]   Bruce Fischl and Anders M. Dale. "Measuring the thickness of the human cerebral cortex from magnetic resonance images". In: *Proc Natl Acad Sci U S A* 97.20 (Sept. 26, 2000), pp. 11050–11055.

[48]   Sunil D. Sharma et al. "Age-related variability in pediatric scalp thickness: Implications for auditory prostheses". In: *International Journal of Pediatric Otorhinolaryngology* 130 (Mar. 1, 2020), p. 109853.

[49]   Zhigang Li et al. "A Statistical Skull Geometry Model for Children 0-3 Years Old". In: *PloS one* 10 (May 18, 2015), e0127322.

[50]   *American National Standard for Safe Use of Lasers. ANSI Z136.1.* 2022.

[51]   W. Riley and W. Klein. ""Piezo-optic coefficients of liquids". In: *The Journal of the Acoustical Society of America* 42.6 (1967), pp. 1258–1261.